Design of Advanced Composite Skins for Morphing Wings - Analysis, Manufacturing, and Control

Yun, Gunjin
SEOUL NATIONAL UNIVERSITY
599 GWANAK-RO, GWANAK-GU
SEOUL, , 151742
KOR

08/31/2021
Final Technical Report

Air Force Research Laboratory
Air Force Office of Scientific Research
Asian Office of Aerospace Research and Development
Unit 45002, APO AP 96338-5002

REPORT DOCUMENTATION PAGE

Form Approved
OMB No. 0704-0188

1. REPORT DATE *(DD-MM-YYYY)*	**2. REPORT TYPE**	**3. DATES COVERED** *(From - To)*
31-08-2021	Final	30 Sep 2017 - 29 Sep 2020

4. TITLE AND SUBTITLE
Design of Advanced Composite Skins for Morphing Wings - Analysis, Manufacturing, and Control

5a. CONTRACT NUMBER
FA2386-17-1-4081

5b. GRANT NUMBER

5c. PROGRAM ELEMENT NUMBER

6. AUTHOR(S)
Gunjin Yun

5d. PROJECT NUMBER

5e. TASK NUMBER

5f. WORK UNIT NUMBER

7. PERFORMING ORGANIZATION NAME(S) AND ADDRESS(ES)
SEOUL NATIONAL UNIVERSITY
599 GWANAK-RO, GWANAK-GU
SEOUL, 151742
KOR

8. PERFORMING ORGANIZATION REPORT NUMBER

9. SPONSORING/MONITORING AGENCY NAME(S) AND ADDRESS(ES)
AOARD
UNIT 45002
APO AP 96338-5002

10. SPONSOR/MONITOR'S ACRONYM(S)
AFRL/AFOSR IOA

11. SPONSOR/MONITOR'S REPORT NUMBER(S)

12. DISTRIBUTION/AVAILABILITY STATEMENT
A Distribution Unlimited: PB Public Release

13. SUPPLEMENTARY NOTES

14. ABSTRACT
Final report covers the topics of: Design criteria for aircraft morphing wing skin, A new concept for morphing wing skin, Morphing mechanism, Topology optimization by targeting prescribed nonlinear stress-strain relationships, Hyperelastic material modeling for elastomeric skin materials, Design and Manufacturing of Variable Camber Morphing Wing, and Analysis of Variable Camber Morphing Wing Skin.
Work resulted in 4 journal papers, 6 International conference presentations, 8 domestic conference presentations, and one award.

15. SUBJECT TERMS

16. SECURITY CLASSIFICATION OF:			**17. LIMITATION OF ABSTRACT**	**18. NUMBER OF PAGES**	**19a. NAME OF RESPONSIBLE PERSON**
a. REPORT	**b. ABSTRACT**	**c. THIS PAGE**			JEREMY KNOPP
			SAR	0	**19b. TELEPHONE NUMBER** *(Include area code)* 315-227-7006

DESIGN OF ADVANCED COMPOSITE SKINS FOR MORPHING WINGS - ANALYSIS, MANUFACTURING, AND CONTROL

Award number: FA2386-17-1-4081

To:

Dr. Jeremy Knopp and Dr. Jaimie S. Tiley

AOARD and AFOSR

December 28 2020

From:

Dr. Gunjin Yun

Department of Mechanical & Aerospace Engineering
Seoul National University, Seoul, South Korea, 08826

Abstract

<table>
<tr><td>Principal Investigator</td><td>Department of Mechanical & Aerospace Engineering Seoul National University</td><td>Full professor</td><td colspan="2">Gunjin Yun</td></tr>
<tr><td>Title of Project</td><td colspan="4">Design of Advanced Composite Skins for Morphing Wings
– Analysis, Manufacturing, and Control</td></tr>
<tr><td>Research period</td><td colspan="2">10/1/2017 ~ 09/30/2020</td><td>Selected Year</td><td>2017</td></tr>
<tr><td>Summarized research work & performance</td><td colspan="4">● Design criteria for aircraft morphing wing skin
● A new concept for morphing wing skin
● Morphing mechanism
● Topology optimization by targeting prescribed nonlinear stress-strain relationships
● Hyperelastic material modeling for elastomeric skin materials
● Design and Manufacturing of Variable Camber Morphing Wing
● Analysis of Variable Camber Morphing Wing Skin
● Journal paper: 4 (4 accepted)
● International conference: 6
● Domestic conference: 8
● Award: 1</td></tr>
</table>

Table of Contents

1 RESEARCH OBJECTIVES AND BACKGROUND

The theory behind altering the wing's geometry, known as the "wing morphing," will lead to improved performance and efficiency of the vehicle's entire flight. The concept of morphing wing has still been evolved to achieve innovation in aircraft flight performance—adaptive changes of aircraft wing by morphing help increase aircraft's fuel efficiency. Removing conventional control surfaces such as fillet, flap by morphing wing concept can reduce aeroacoustics and noises. Aircraft wing morphing according to the flight conditions has several variations. For example, sweep, chord, span, camber geometry change. VCCW (Variable Camber Compliant Wing) has an advantage in maintaining morphed shapes enabled by conventional actuators, unlike smart materials. The VCCW developed by AFRL was designed and fabricated based on compliant mechanism and advanced 3D additive manufacturing technologies with the other surface process[1, 2] [1, 2]. The VCCW morphing concept objects to change the camber shape freely according to the flight situation.

When we consider any morphing wing structures and controls, an important parameter is often overlooked: the skin for the wing. When the wing morphs, the skin for morphing must be soft enough to allow shape changes, but at the same time, it must be stiff enough to withstand the aerodynamic and structural loads and maintain the required shape or profile under various flight modes.

The main objectives of this project are (1) to design compliant and multi-dimensional and functional advanced composite skins considering morphing wings' mechanical/structural, geometrical, and aerodynamic characteristics, (2) to design and implement mesostructured morphing skins using 3D additive manufacturing technology, (3) to establish and validate a rapid design process of skins for various types of morphing, and (4) to implement control parameters to materials for active control of manufactured skins.

The research plan of the proposal is as follows.

Table. 1: Research plan of the proposal

	Plan	
1st year	Objectives ● To design compliant and multi-dimensional and functional advanced composite skins considering morphing wings' mechanical/structural, geometrical, and aerodynamic characteristics	Task 1-1 Development of Karhunen-Loeve-Expansion(KLE)-based finite element morphing wing model
		Task 1-2 Development of macro-scale material topology optimization method and tool
		Task 1-3 Project meetings and collaboration plans
2nd year	Objectives ● To design and implement mesostructured morphing skins using 3D additive manufacturing technology	Task 2-1 Mesostructure topology optimization with cellular honeycomb
		Task 2-2 Mesostructure topology optimization with auxetic honeycomb
		Task 2-3 3D additive manufacturing of the optimized mesostructure

		Task 2-4 Project meetings
3rd year	Objectives ● To establish and validate a rapid design process of skins for variou s types of morphing	Task 3-1 Laboratory experimental tests
		Task 3-2 Fluid-structure interaction (FSI) simulation
		Task 3-3 Manufacturing of full-scale morphing skin and wind tunnel test
		Task 3-4 Project meeting for final reports

2 RESEARCH CONTENTS AND RESULTS

2.1 A New Concept for Morphing Wing Skin

2.1.1 Decoupled In-Plane and Out-of-Plane Mechanisms of Gripper Pin

For aircraft morphing wing skins, a gripper pin structure is proposed, a new concept that separates in-plane and out-of-plane stiffness. Fig. 1 shows the schematics of the gripper-pin. The T-shaped end of the gripper pin is slotted into the groove of an adjacent gripper pin. Multiple gripper pins are connected serially by this slot connection. The large clearance within the slot determines the range of motion in the x-direction. Contact friction-dependent in-plane stiffness can realize low actuation energy, a unique feature of the proposed wing skin. On the contrary, bending stiffness around x and y-axis of the unit gripper pin is high enough to withstand aerodynamic loadings.

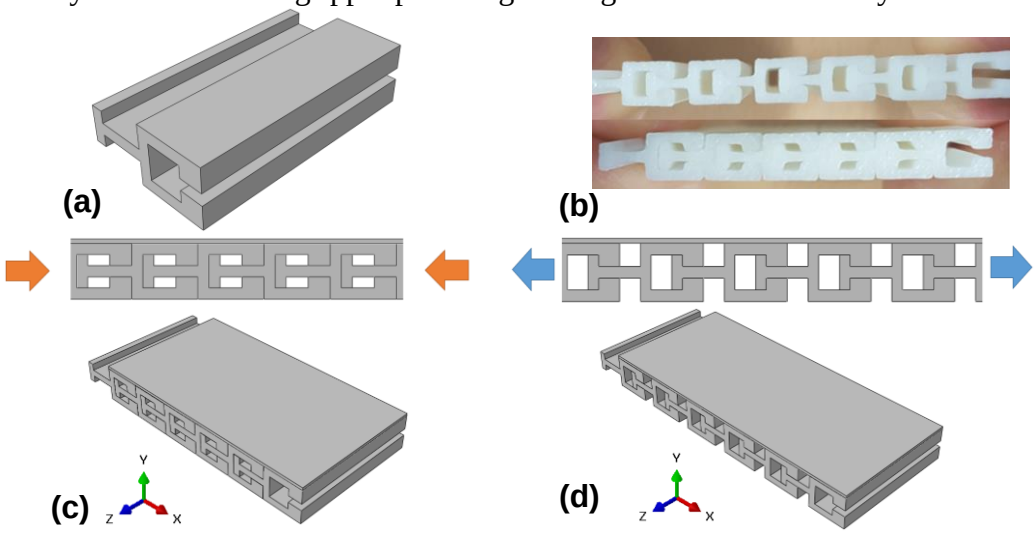

Fig. 1 Gripper pin structure: (a) unit pin; (b) 3D printed structure; (c) structure under compression; (d) structure under tension.

Fig. 2 depicts two design parameters (i.e., δ and t) of the gripper pin structure. The geometry of the gripper pin is determined by altering the design parameters, δ, and t.

y

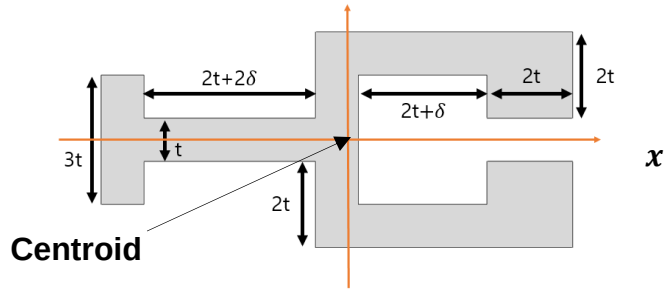

Fig. 2 Design parameters (i.e., δ and t) of gripper pin structure.

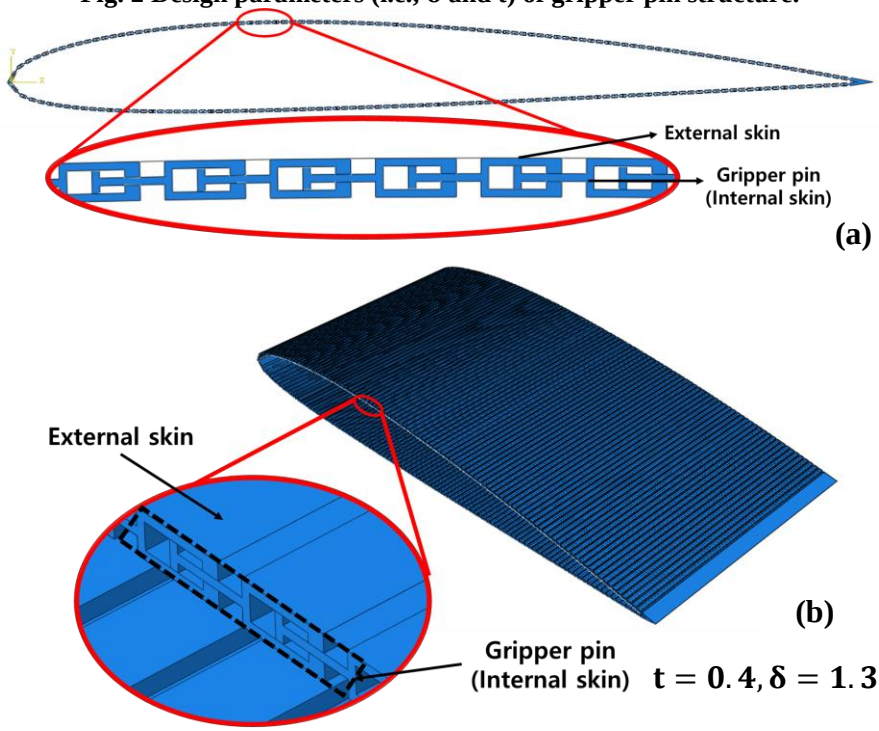

Fig. 3 Gripper pin wing skin: (a) spar direction (b) three-dimensional view.

2.1.2 Analytical Analysis of the Gripper Pin Structure

During the morphing process and flight conditions, the aircraft wing is subjected to morphing loading and aerodynamic lift force resulting in combined loadings, flexural moment, shear force, and torsional moment. Serial connections by slotting a T-shaped end into the groove can assume that the torsional rigidity of the airfoil is a sum of the torsional rigidities of all individual gripper pins. This because the gripper pin skin is not a closed section but consists of the gripper pin units, which are open sections. Therefore, the torsional rigidity of the gripper pin skin is determined in Eq. **(1)**

$$H_{zz} = \sum_{i=1}^{Ng} H_{zz}^{(i)} \text{ and } H_{zz}^{(i)} = \frac{G(44t+6\delta)t^3}{3} \quad (1)$$

where G is the shear modulus; L is the length of the curve, and t is the thickness of the wall.

Understanding the interaction between gripper pins is a crucial step for designing the gripper pin. Fig. 4 shows the interaction between the gripper pins. The gripper pins are coupled to each other in a fit-in manner, and sliding occurs at the interface. There are two interaction forces

between gripper pins: shear friction force and normal force at the contact surfaces as shown in Fig. 4.

$$F_s^{(i,j)} = \mu N^{(i,j)}, F_n^{(i,j)} = N^{(i,j)} \quad (2)$$

where $F_s^{(i,j)}$ and $F_n^{(i,j)}$ are the shear friction and the normal forces acting on the gripper pin's contact surface, respectively, and μ is the friction coefficient.

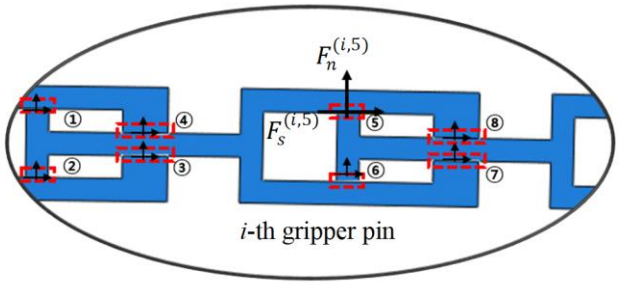

Fig. 4 Interaction forces between gripper pins.

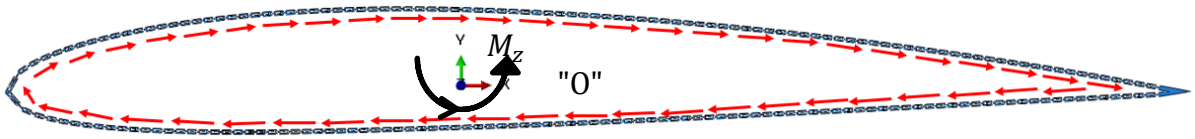

Fig. 5 Shear flow on the cross-section of the gripper pin skin.

Fig. 5 shows the shear flow on the cross-section of the gripper pin skin. Depending on the tolerance, the friction forces could be considerable. Then the total torque M_z about the reference point an "O" of airfoil is obtained as follows

$$M_z = \sum_{i=1}^{N_g-1}\sum_{j=1}^{N_{cs}}\left(r_{0s}^{(i,j)}F_s^{(i,j)} + r_{0n}^{(i,j)}F_n^{(i,j)}\right) + \sum_{j=1}^{N_{cs}-4}\left(r_{0s}^{(N_g,j)}F_s^{(N_g,j)} + r_{on}^{(N_g,j)}F_n^{(N_g,j)}\right) \quad (3)$$

where $r_{0s}^{(i,j)}$ is the perpendicular distance from the reference point "O" to the line of friction force $F_s^{(i,j)}$ and $r_{0n}^{(i,j)}$ is the perpendicular distance from the reference point "O" to the line of the normal force $F_n^{(i,j)}$, N_g is the number of gripper pin units, and N_{cs} is the number of contact surfaces of one gripper pin, which is eight in our design. Each gripper pin is a thin-walled open section subjected to shear forces, $V_x^{(i)}$and $V_y^{(i)}$, which are in equilibrium with friction and normal forces as follows

$$V_x^{(i)} = \sum_{j=1}^{N_{cs}} F_s^{(i,j)} \text{ and } V_y^{(i)} = \sum_{j=1}^{N_{cs}} F_n^{(i,j)} \quad (4)$$

These shear forces give rise to shear flow distribution along with the thin-walled segments of the gripper pin. Depending on the loading condition, the equivalent shear forces can be set off from the shear center. The shear center is along the symmetric line in the x-direction. The offset distance of the shear force positions from the shear center gives rise to torsion, $T^{(i)} = V_x^{(i)}(e_y - d_y) + V_y^{(i)}(e_x - d_x)$ where e_x and e_y are the locations of the shear center and d_x and d_y are locations of the shear forces.

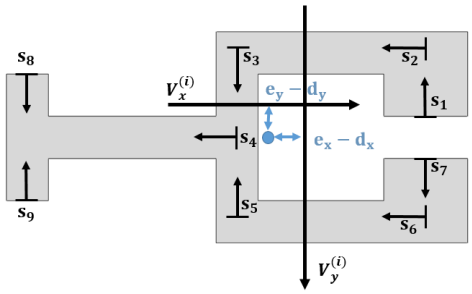

Fig. 6 Curvilinear coordinate systems on gripper pin.

2.1.3 3D Finite Element Model Analysis

A special and unique FE model for the actuator section was developed to induce camber and wing profile changes. However, this model does not represent actual mechanisms inside of the VCCW model. As shown in Fig. 7, the model has equally spaced cuts like fish-bone to allow free shaping to any NACA profile. Fig. 7(a) represents the displacement contour after morphing to the target shape (NACA8410). As shown in Fig. 7(b) and (c), the developed FE model has achieved the wing profile, and the camber line is perfectly matched with the targeted ones. Hence, the proposed model is advantageous for morphing analysis and skin design.

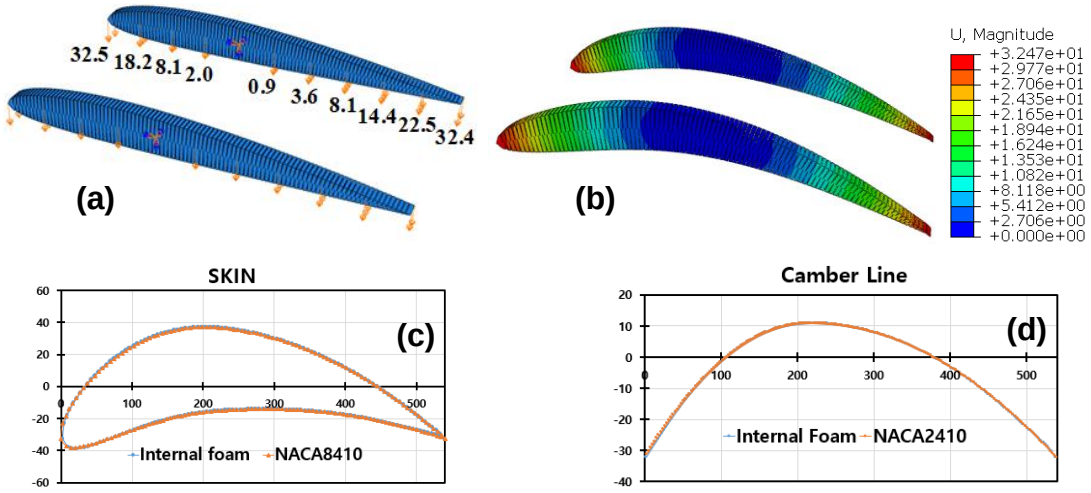

Fig. 7: Deformation of actuator; (a) Load and boundary condition (b) after morphing to NACA 8410, actuator section (c) wing profile (d) camber line

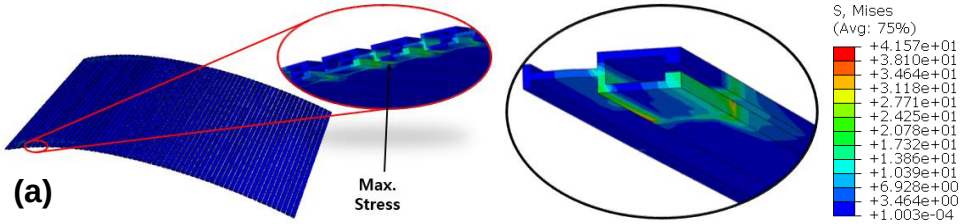

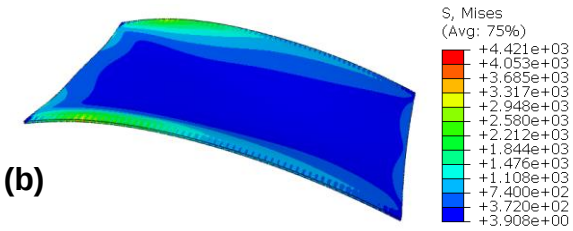

Fig. 8 Stress Contour: (a) gripper pin wing skin (b) bulk material skin.

Fig. 8 shows the von Mises stress distribution of the gripper pin wing skin and bulk material wing skin. The gripper pin wing skin's maximum stress level was a hundred times smaller than that of the bulk material. The safety factor is also critical to verify the structure's validity and prevent damage to the material. Considering aluminum's yield stress, 290 MPa, the gripper pin wing skin showed no failure and safety factor 6.98 while the bulk material skin's maximum stress exceeded aluminum yield stress level. On the other hand, the bulk material wing skin's stress distribution was concentrated at the portion attached to the actuator section, while the gripper pin wing skin showed extremely low-stress level on the entire surface of the wing skin. This stress distribution feature implies that the actuation energy level of the gripper pin wing skin is small.

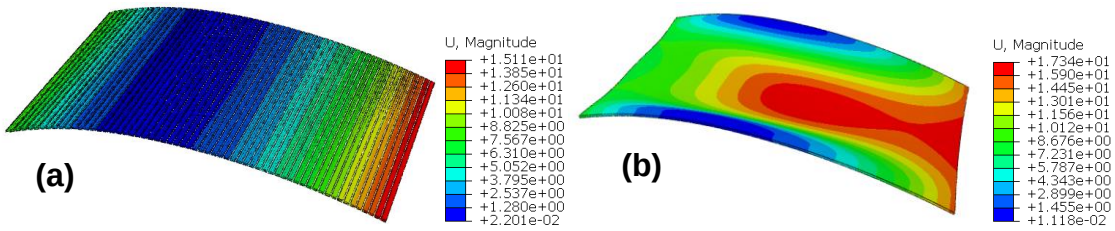

Fig. 9 Displacement contour: (a) gripper pin wing skin (b) bulk material skin.

Displacements of the wing skin were also compared as depicted in Fig. 9 to see the irregular out-of-plane deformation occurring on the wing skin's surface. The irregular out-of-plane deformation will lead the flow separation and eventually pose a negative influence on the skin's aerodynamic performance. Therefore, irregular out-of-plane deformation is undesirable. As shown in Fig. 9 (a), the gripper pin's out-of-plane deformation was extremely low compared to that of the bulk material skin. Although maximum displacement of the skin was similar, the gripper pin skin's out-of-plane deformation was uniform along the spar direction partly due to high out-of-plane stiffness while the bulk material skin showed sagging out-of-plane deformation. It is also partly due to the sliding mechanism of the gripper pin.

2.2 Morphing Mechanism

2.2.1 Scissors Structure System Modeling

We considered a way to construct an internal morphing mechanism with a scissors structure. Deployable scissors structure is a structure with a wide range of applications that requires various curvatures and forms. Revolute joints connect the scissors structure system, and the length between joints has a constraint condition.

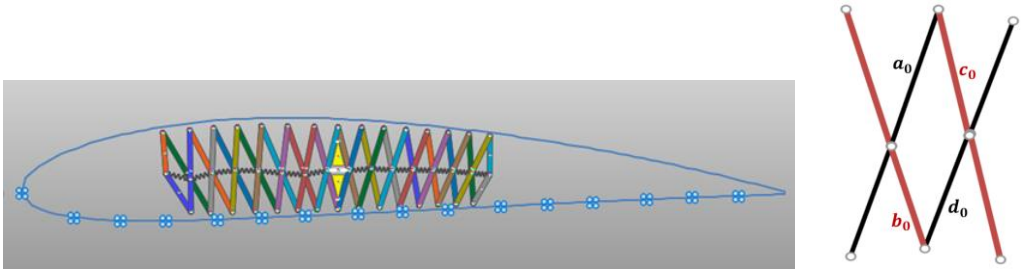

Fig. 10 (a) Scissors Structure inside the airfoil (b) Scissors deployability constraint

For the scissors structure to be deployable like Fig. 10, which shows a part of the scissors structure system where four elements are connected through 4 joints, it has to satisfy the deployable condition $a_0 + b_0 = c_0 + d_0$ [3]. One scissor is defined as a unit [4]. The deployment form of scissors structure is decided by each unit's measurements (length, angle). As general scissors structure has one degree of freedom once the length of units composing the structure is fixed, the degree of freedom was set up as an arbitrary scissors unit's angle.

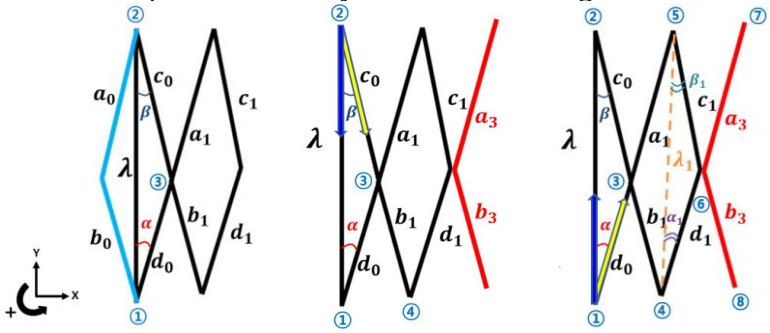

Fig. 11 Schematics of scissors (a) center (b) angle beta (c) angle alpha

2.2.2 Scissors Structure Airfoil Optimal Design

Left and right is divided by the base/reference line ①-② in Fig. 11. Quadrangle, including the baseline, was made symmetrical, and point ① in Fig. 11 is considered as fixed coordinate. β is obtained through the triangle consisting of point ①, ②, and ③. (λ is defined as the length between point ① and ②.) A vector from point ② to point ④ can be obtained by rotating a vector with a direction of point ① toward point ②, and a magnitude of 1 by β, and then multiplying $(c_0 + b_1)$. By rotating a vector with a direction of point ① toward ②, and a magnitude of 1 clockwise by α, and then multiplying $(d_0 + a_1)$, vector from point ① to ⑤ can be obtained. The calculation was done by Matlab, and if repeatably done, the right coordinates forming scissors structure system is calculated. In the case of the left coordinates, all is the same as above except that α_n $(n = 1,2, \dots)$ should be rotated counter clockwise and $\beta_n (n = 1,2, \dots)$ clockwise. Consequently, we can find out that deployment forms of scissors structure change as the input angle α differs.

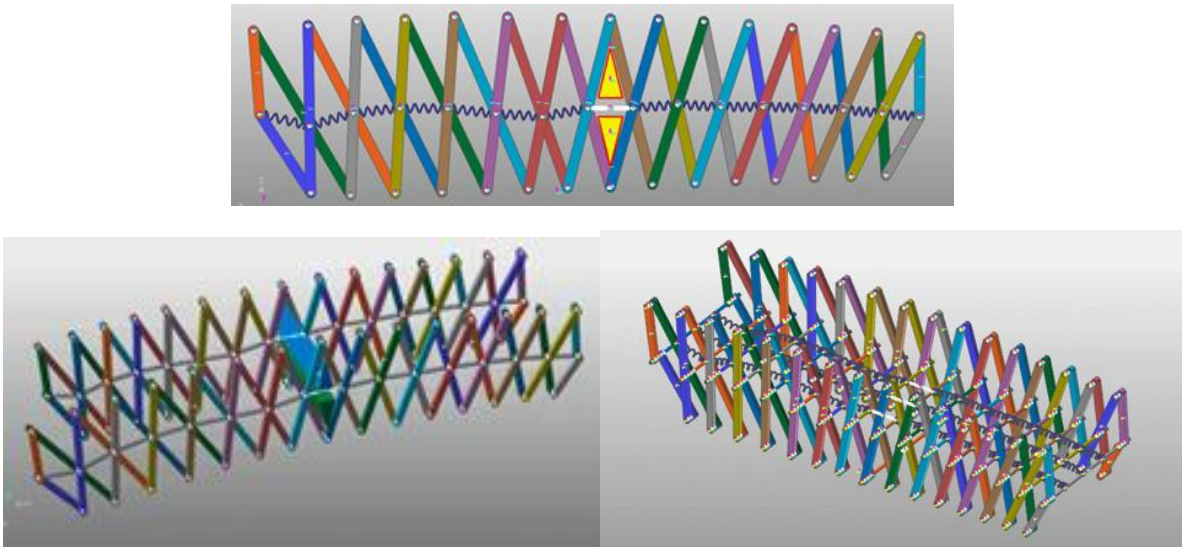

Fig. 12 Various Modelings of Scissors Deployable Airfoils

Using the obtained results, we modeled the scissors structure like Fig. 12. We added the driving force that pushes both sides from the middle and considered gravity as the power besides the driving force. Besides, we designed various models to reinforce the structure's stiffness and found that these scissors structured-airfoil models implement various airfoil forms through dynamic simulation.

2.2.3 Scissors Structure's Dynamic Simulation

Optimization finding input angle α that minimizes total sum of the length between the actual airfoil coordinates $[x_{ra}, y_{ra}, z_{ra}]_n$ (n = 1,2, …) and the scissor airfoil coordinates $[x_{sc}, y_{sc}, z_{sc}]_n$ $(n = 1, 2, \dots)$ (that are formed by deployable scissors structure obtained through implementing methods above) was implemented. First, there needs to be a standard about what points should be matched to the actual airfoil coordinates and scissors structure coordinates, respectively. In this paper, the standard was made so that among numerous points that form actual airfoil, x_{ra} , which has less than 0.1% error compared to the scissors structure's x-coordinate x_{sc}, can be matched. If there are more than 2 x_{ra} that have less than 0.1% error, the one with less error is selected. The smaller the total sum of the length between corresponding points is, the more approximate the scissors structure is. In a result, the input angle α that minimizes the total sum can be found. Matlab did the calculation of optimum design process. To simulate that the airfoil constructed with scissors structure system changes into its demanding airfoil form as input angle alters, dynamic simulation software Recurdyn was used.

2.3 Topology Optimization by targeting prescribed nonlinear stress-strain relationships

We proposed a microstructure topology optimization methodology in a 3D continuum material domain with material nonlinearity considered, targeting the prescribed stress-strain curves. This method has a novelty in that it can create microstructure topology targeting nonlinear stress-strain curves rather than targeting specific properties, for example, stiffness or strength. The sensitivity considering the elastoplastic material behavior was formulated and implemented by the adjoint

method. For a demonstration of the proposed method, 3D microstructures were obtained by error minimization of the targeted effective stress-strain curve for both cases of uniaxial tensile test and biaxial tensile test.

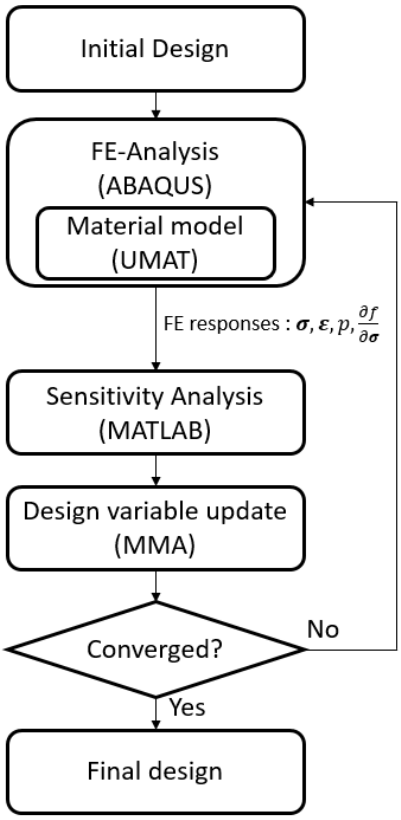

Fig. 13 Overall flow chart of the optimization

2.3.1 Optimization formulation

For material design, we focus on the microstructure topology of representative volume element (RVE), assuming that bulk material properties are known a priori. The targeted nonlinear constitutive behavior of the RVE is defined in terms of prescribed effective stress-strain curves. The volume-averaged von Mises effective stress is computed value as

$$\tilde{\sigma}_e = \frac{\sum_{i=1}^{N_{gp}} \sigma_{e\_i} \times V_i}{\sum_{i=1}^{N_{gp}} V_i} = \frac{\sum_{i=1}^{N_{gp}} \sigma_{e\_i} \times \det(J_i)}{\sum_{i=1}^{N_{gp}} \det(J_i)} \tag{5}$$

where $\sigma_{e\_i} = \sqrt{\frac{1}{2}[(\sigma_{11}-\sigma_{22})^2 + (\sigma_{11}-\sigma_{33})^2 + (\sigma_{22}-\sigma_{33})^2 + 6(\sigma_{12}^2+\sigma_{13}^2+\sigma_{23}^2)]}$

σ_{e_i} is the effective stress at *i*-th Gauss point, N_{gp} is the total number of Gauss points within RVE design domain, and V_i is the elemental volume which is identical to the determinant of the elemental Jacobian (J_i). Using volume-averaged effective stress in the objective function is to

compute the sensitivity in the design domain with the periodic boundary condition (PBC), which is described later in this section. The objective function with constraints is expressed as:

$$\min c(\rho_e) = \sum_{n=1}^{N_{inc}} \left({}^{n}\sigma_e^{target} - {}^{n}\tilde{\sigma}_e \right)^2$$

$$\text{such that } \sum_{e=1}^{N_e} v_e \rho_e \leq V$$

$$0 \leq \rho_e \leq 1, \quad e = 1, \dots, N_e$$

$$\text{with the coupled residuals } {}^{n}\mathbf{R}({}^{n}\mathbf{v}) = \widehat{f_{ext}} - \int B^T \sigma_i dV = 0, \tag{6}$$

$$n = 1, \dots, N_{inc}$$

$${}^{n}\mathbf{H}\left({}^{n}\mathbf{u}, {}^{n-1}\mathbf{u}, {}^{n}\mathbf{v}, {}^{n-1}\mathbf{v}, \rho_e\right)$$

$$= \begin{bmatrix} B(u_n - u_{n-1}) - D^{-1}(\sigma_n - \sigma_{n-1}) - \dfrac{\partial f}{\partial \sigma_n}(\lambda_n - \lambda_{n-1}) \\ \sqrt{3J_2} + \alpha I_1 - \sigma_y(\lambda_n) \end{bmatrix} = 0 ,$$

$$n = 1, \dots, N_{inc}$$

$$\text{where, } {}^{n}\mathbf{v} = \begin{bmatrix} {}^{n}\boldsymbol{\sigma} \\ {}^{n}p \end{bmatrix}$$

where V is the total volume of the design domain and N_{inc} is the total number of target points, that is, incremental steps. ${}^{n}\mathbf{R}$ and ${}^{n}\mathbf{H}$ are global and local residuals, respectively, that must be satisfied in the nonlinear finite element analysis. Therefore, ${}^{n}\mathbf{R}$ must be solved at the global level and ${}^{n}\mathbf{H}$ at the Gauss point level. Since we neglect body forces, the global residual ${}^{n}\mathbf{R}$ is explicitly expressed only on ${}^{n}\mathbf{v}$.

2.3.2 Verification of the proposed sensitivity analysis

The sensitivity of the objective function is compared with the sensitivity obtained by the finite difference method (FDM) to verify its accuracy. FDM requires a large number of computations, thus we create a simple model with a small number of elements. The domain is discretized into $3 \times 3 \times 3$ elements. In this size, the target microstructure is shown in Fig. 14. In the initial design, only one element in the center of the domain is empty, and based on this, and sensitivity analysis is carried out. The FDM equation is as follows:

$$\nabla_{\rho_j} f = \frac{f(\rho + \Delta\tilde{\rho}) - f(\rho)}{\Delta\rho_j} \tag{7}$$

$$\text{where } \Delta\tilde{\rho}_i = \delta_{ij}\Delta\rho_j$$

where $\Delta\tilde{\rho}$ is a vector with all components zero except the j-th component, and $\Delta\rho_j$ is a finite perturbation of the design variable. In this study, the value of finite perturbation $\Delta\rho_j$ is 1.0×10^{-3}. The sensitivity obtained from FDM and the sensitivity computed from the proposed method are compared in Fig. 15. These two sensitivities are almost identical, with a maximum error of 0.5 percent. In this way, we verified that the proposed method's sensitivity and confirmed that they could be applied to problems considering material nonlinearity with high accuracy.

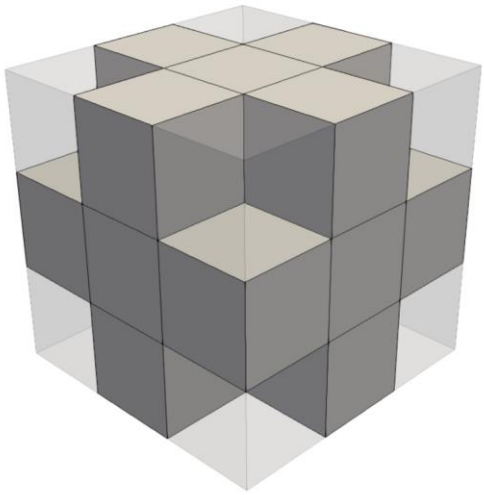

Fig. 14 Pseudo material for verification

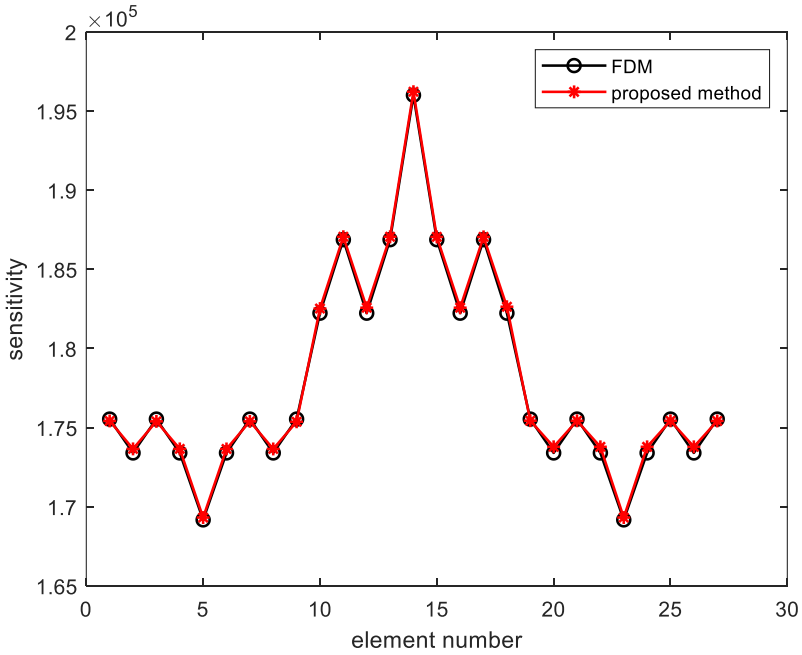

Fig. 15 Comparison FDM and the proposed method

2.3.3 Test results

We performed the topology optimization to minimize the difference of nonlinear volume-averaged effective stress-strain between the target microstructure and the design candidates. Target nonlinear properties are responses obtained from arbitrary pseudo materials. In the first case, the RVE design domain is strained with a range [0,0.01] in the x-direction. In the second case, a monotonic strain with a range of [0, 0.01] was applied in x and y directions as a boundary condition. During optimization, the sensitivity and design variables are updated.

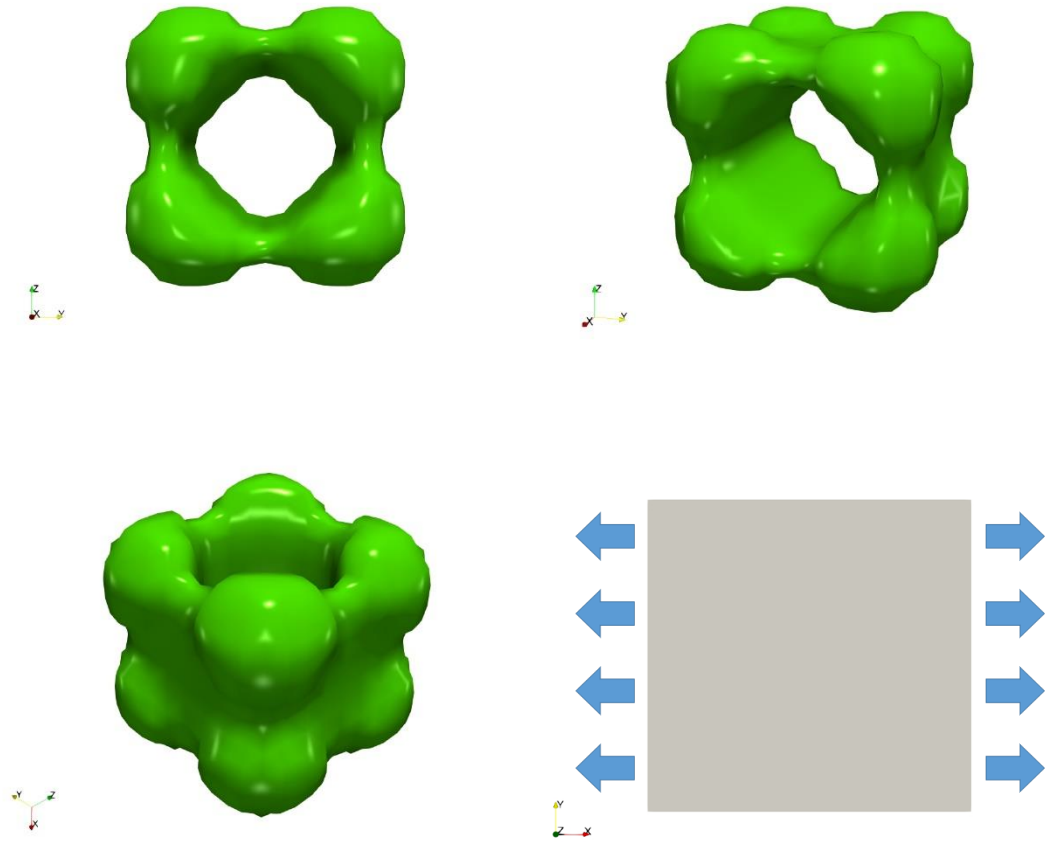

(a)

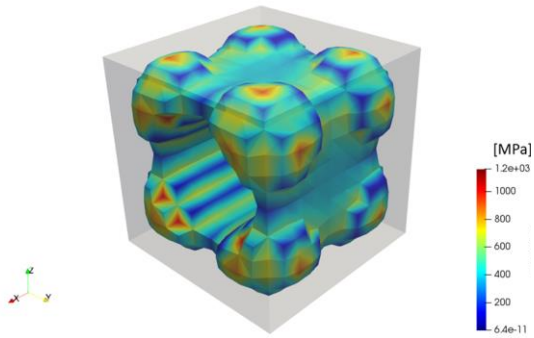

(b)

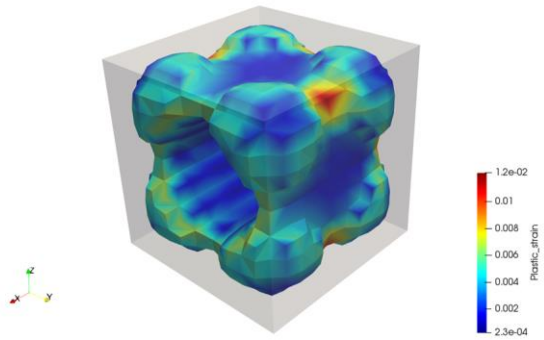

(c)

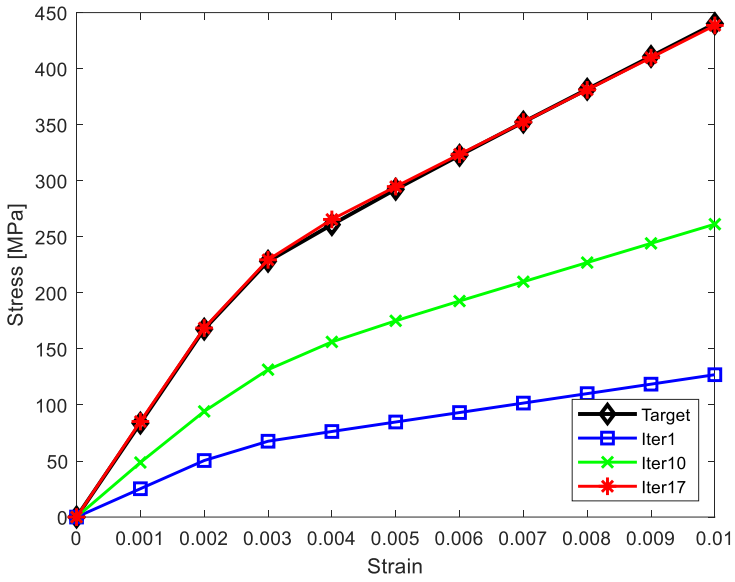

(d)

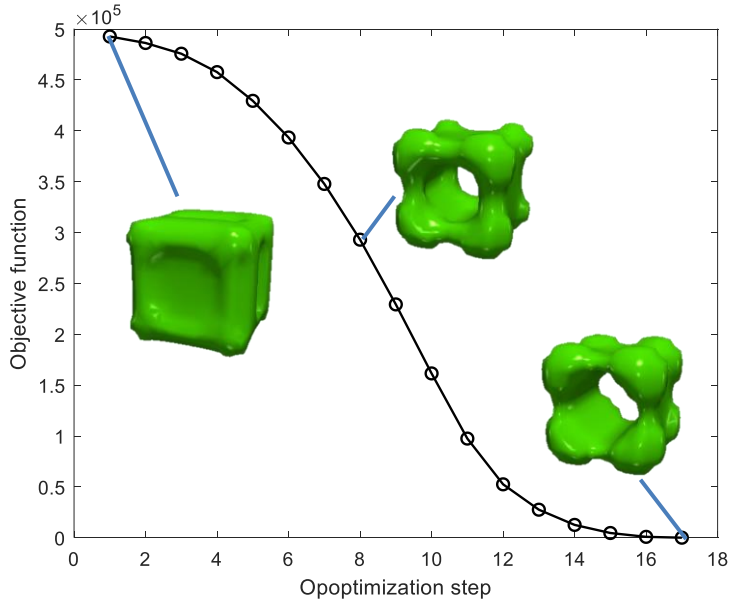

(e)

Fig. 16 (a) Final design of RVE microstructure targeting nonlinear stress-strain response and boundary condition (b) von Mises equivalent stress (c) equivalent plastic strain (d) volume-averaged effective stress-strain curve (e) changes of the objective function values

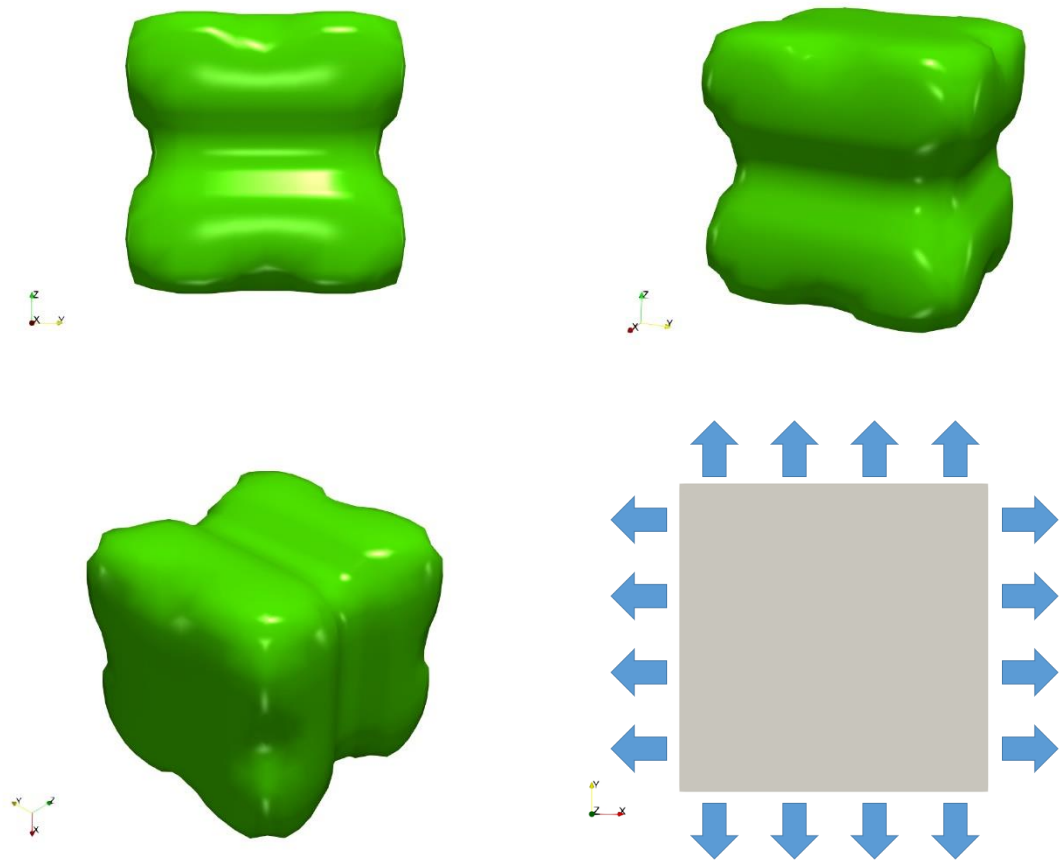

(a)

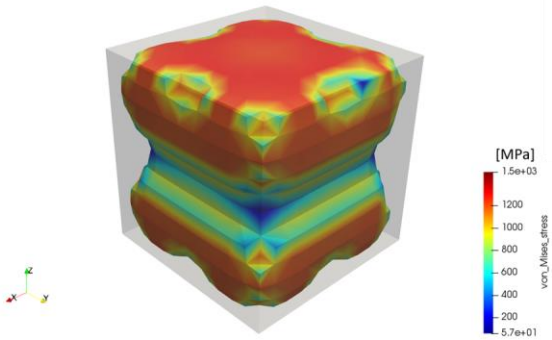

(b)

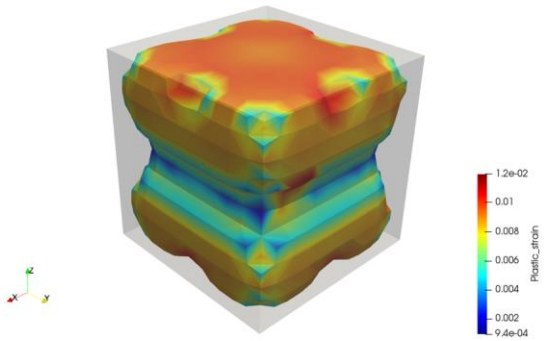

(c)

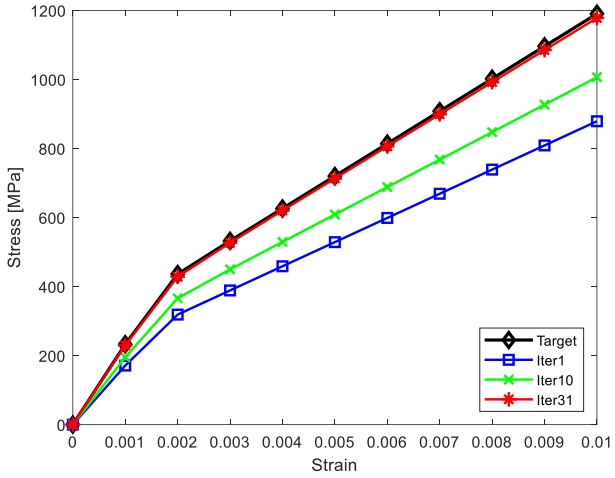

(d)

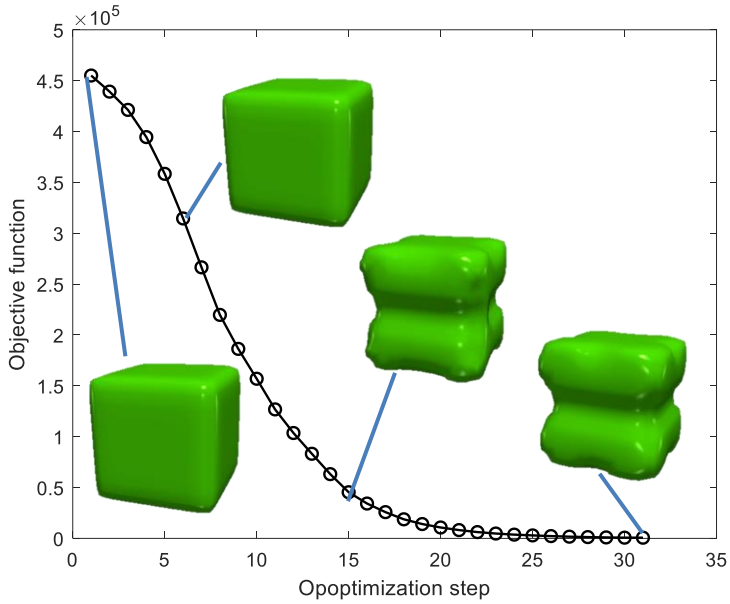

(e)

Fig. 17 (a) Final design of RVE microstructure targeting nonlinear stress-strain response and boundary condition (b) von Mises equivalent stress (c) equivalent plastic strain (d) volume-averaged effective stress-strain curve (e) changes of the objective function values

2.4 Hyperelastic material modeling

We developed a hyperelastic material model to apply the topology optimization design frame described in the previous section to the elastomeric material to be used for the wing skin. The material model was developed as a user material subroutine of ABAQUS (UMAT). The subroutine has been developed in a general form to be applied to any potential energy defined as a strain invariant. Therefore, if the strain energy potential can be differentiated as a strain invariant, it can

be used. The following equation is the consistent tangent stiffness derived from any strain energy potential.

$$
\begin{aligned}
\mathrm{C} = & \frac{2}{J}\frac{\partial \bar{W}}{\partial \bar{I}_1}\left(\mathbf{1} \lozenge \mathrm{dev}(\bar{\mathbf{B}}) + \mathrm{dev}(\bar{\mathbf{B}}) \lozenge \mathbf{1} + \frac{2}{3}\bar{I}_1(\mathbf{I} - \frac{1}{3}\mathbf{1} \otimes \mathbf{1}\right) \\
& -\frac{2}{3}(\mathbf{1} \otimes \mathrm{dev}(\bar{\mathbf{B}}) + \mathrm{dev}(\bar{\mathbf{B}}) \otimes \mathbf{1})] \\
& + \frac{2}{J}\frac{\partial \bar{W}}{\partial \bar{I}_1}[-(\mathbf{1} \lozenge \mathrm{dev}(\bar{\mathbf{B}}^{-1}) + \mathrm{dev}(\bar{\mathbf{B}}^{-1}) \lozenge \mathbf{1}) + 2(\bar{\mathrm{B}} \otimes \bar{\mathrm{B}} - \bar{\mathrm{B}} \lozenge \bar{\mathrm{B}}) \\
& + \frac{4}{3}\bar{I}_2(\mathbf{I} - \frac{2}{3}\mathbf{1} \otimes \mathbf{1}) + \frac{4}{3}(\mathbf{1} \otimes \mathrm{dev}(\bar{\mathbf{B}}^{-1}) + \mathrm{dev}(\bar{\mathbf{B}}^{-1}) \otimes \mathbf{1})] \\
& + \frac{4}{J}\left(\frac{\partial^2 \bar{W}}{\partial \bar{I}_1^2}\mathrm{dev}(\bar{\mathbf{B}}) \otimes \mathrm{dev}(\bar{\mathbf{B}}) + \frac{\partial^2 \bar{W}}{\partial \bar{I}_2^2}\mathrm{dev}(\bar{\mathbf{B}}^{-1}) \otimes \mathrm{dev}(\bar{\mathbf{B}}^{-1})\right) \\
& - \frac{4}{J}\frac{\partial^2 \bar{W}}{\partial \bar{I}_1 \bar{I}_2}\left(\mathrm{dev}(\bar{\mathbf{B}}^{-1}) \otimes \mathrm{dev}(\bar{\mathbf{B}}) + \mathrm{dev}(\bar{\mathbf{B}}) \otimes \mathrm{dev}(\bar{\mathbf{B}}^{-1})\right) \\
& + (\frac{\partial U}{\partial J} + J\frac{\partial^2 U}{\partial J^2})\,\mathbf{1} \otimes \mathbf{1}
\end{aligned}
\tag{8}
$$

where $\bar{\mathbf{B}}$ is the left Cauchy-Green deformation tensor, dev( ) is the deviatoric operator, $\mathbf{I}$ is the fouorth order identity tensor, $\mathbf{1}$ is the second order identity tensor and $\lozenge$ is the operator expressed following relation: $\mathbf{I} = \mathbf{1} \lozenge \mathbf{1} = \frac{1}{2}[(\mathbf{1} \otimes \mathbf{1}) + (\mathbf{1} \otimes \mathbf{1})]$.

2.5 Design of Variable Camber Morphing Wing

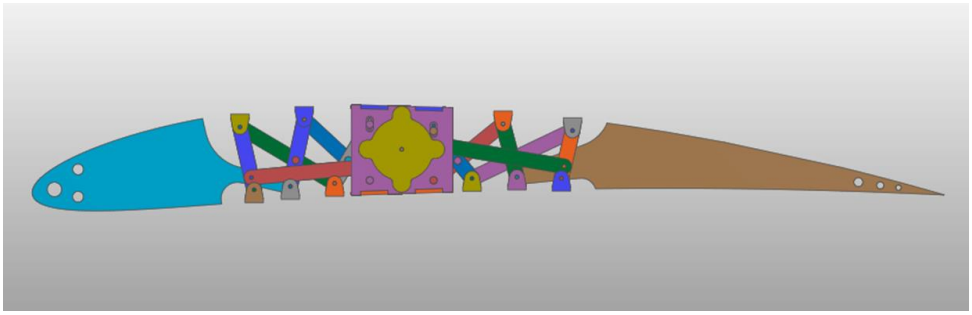

Fig. 18 Developed design of camber morphing wing rib with the deployable structure

The concept design applying the deployable scissor structure is shown in Fig. 12. The developed model was designed to increase the durability and operability of the internal mechanism as shown in Fig. 18.

2.5.1 Modeling of the Wing Rib with Deployable Scissor Structure

To operate the wing rib, the deployability constraint [3] must be satisfied. Through the mathematical model, the coordinates of the structure $[x_{sc}, y_{sc}, z_{sc}]_n$ $(n = 1, 2, \dots)$ can be obtained. The deployable scissor structure of the developed model has the offset parts, as shown in Fig. 19. The offset parts make it possible to generate the surface so that the skin can be attached to the

structure. The offset parts are connected with deployable scissor structure by revolute joints, so they can rotate.

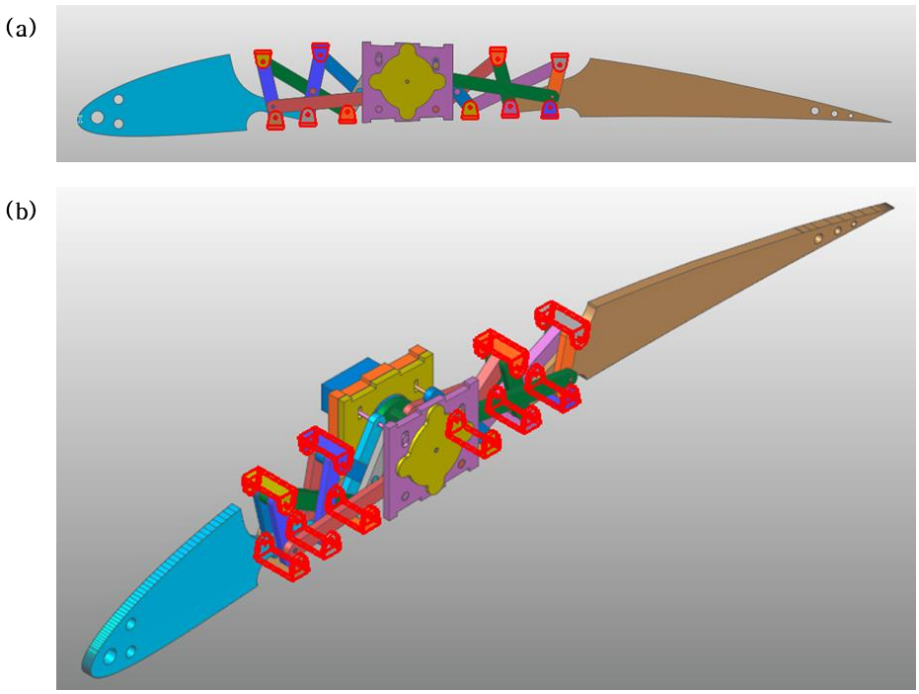

Fig. 19 Offset parts with Camber morphing wing rib

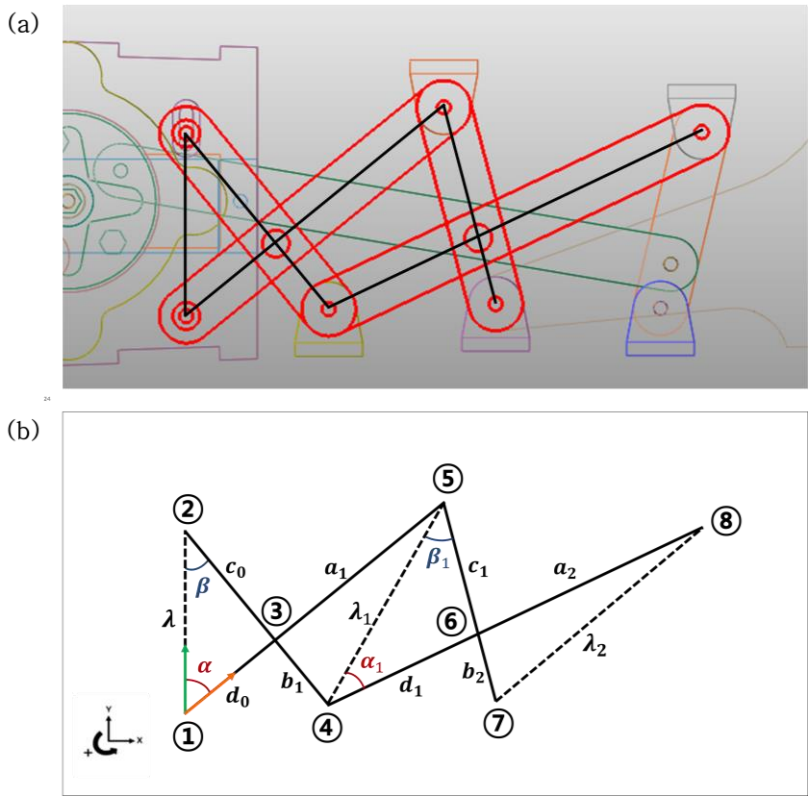

Fig. 20. Deployable Scissor Structure for the right side of the wing

There are differences between the previous model and the developed model. One of the differences is the number of scissor unit because the airfoil's chord length should be kept constant during the deformation. The developed model has three scissor units for each side. Another difference is the connection between the actuator and the deployable scissor structure. The links marked in Fig. 21(a) connect the actuator and the deployable scissor structure. These are not existing for the previous model and connected with a disc. The disc is fixed with the actuator that generates a driving force to deform the rib's shape.

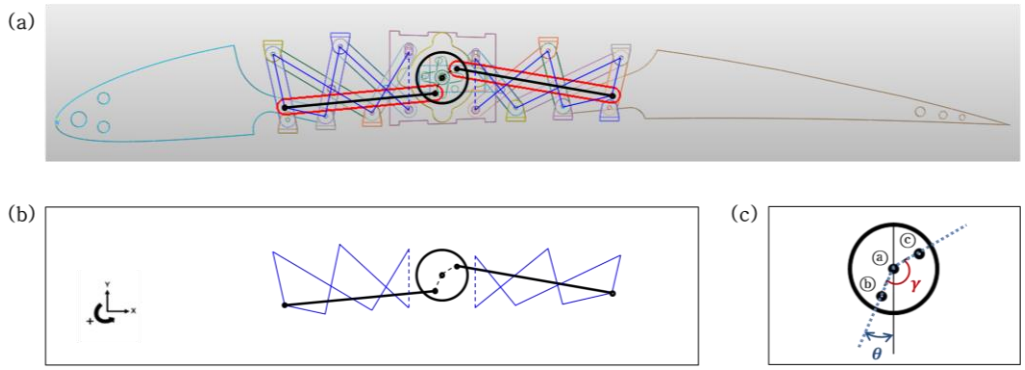

Fig. 21. (a) Actuation links connecting the actuator and the deployable scissor structure, **(b)** The disk connected with the actuator and the lines of the links consisting of wing structure, **(c)** The disk connected with the actuator and the disk's dimension

In Fig. 21(a) and (b), the disc is connected with the leading edge part and the trailing edge part by two links each and has a center as Point ⓐ. These links are connected by two locations as Point ⓑ and Point ⓒ. γ is the angle between these links and is a fixed value. However, the angle θ is a variable vaule. This angle is set as an input parameter of the structure. In other words, the shape of the entire structure is determined by the angle θ.

2.5.2 Optimum Design of Variable Camber Morhping Internal Mechanism

The camber morphing wing rib must deform as the target airfoils accurately. An optimization process can minimize the sum of distances between all target airfoils' coordinates and the deployable scissor structure's coordinates. Since the shape of the deployable scissor structure is determined by the members' dimensions, the dimensions should be set through the optimization process to fit all target shapes. One of the dimensions, the angle θ is set as Table. 1.

Table. 1. Angle θ for the target airfoils

Airfoil / Parameter	NACA 2410	NACA 3410	NACA 4410	NACA 5410	NACA 6410	NACA 7410	NACA 8410
Angle θ	7°	13°	19°	25°	31°	39°	49°

When the angle θ is given for each target airfoil, the optimum design finds the lengths that make the shape difference the smallest. The target airfoils are 4 digit NACA airfoil (NACA 2410, NACA 3410, NACA 4410, NACA 5410, NACA 6410, NACA 7410, NACA8410), and the chord length is set as 500mm. The optimal design process was calculated by Matlab and derived the lengths of the deployable scissor structure. The process is shown in Fig. 22.

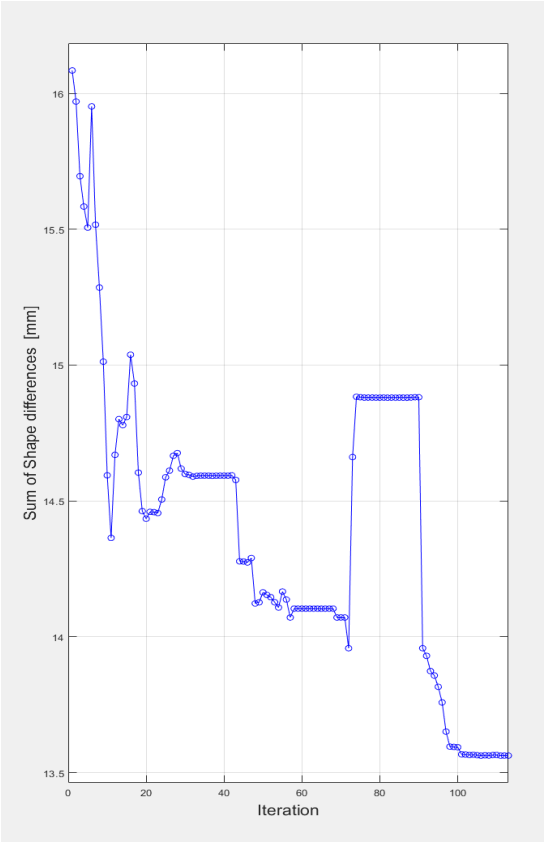

Fig. 22 The sum of the shape difference through the optimization process

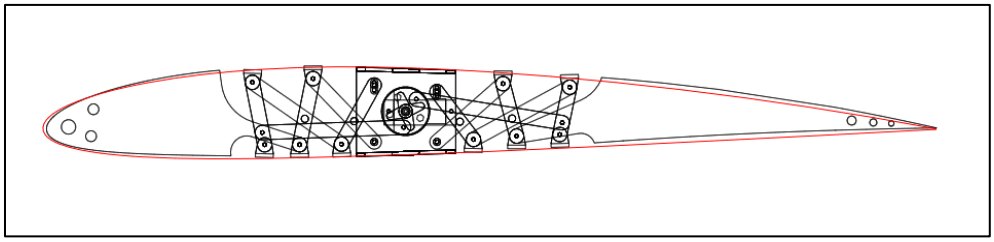

Fig. 23 The shape difference between the morphing wing rib and NACA 2410

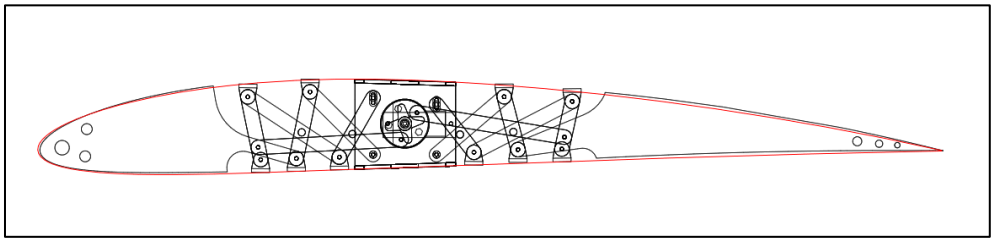

Fig. 24 The shape difference between the morphing wing rib and NACA 3410

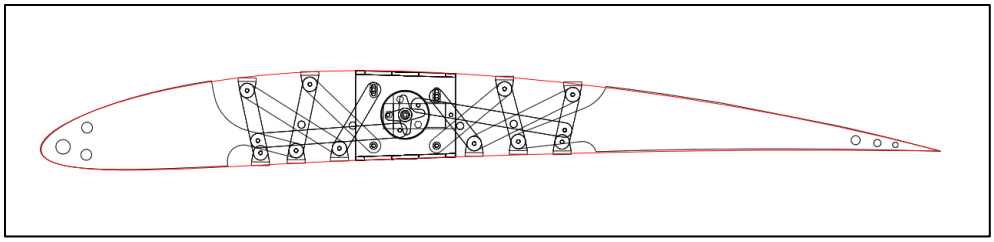

Fig. 25 The shape difference between the morphing wing rib and NACA 4410

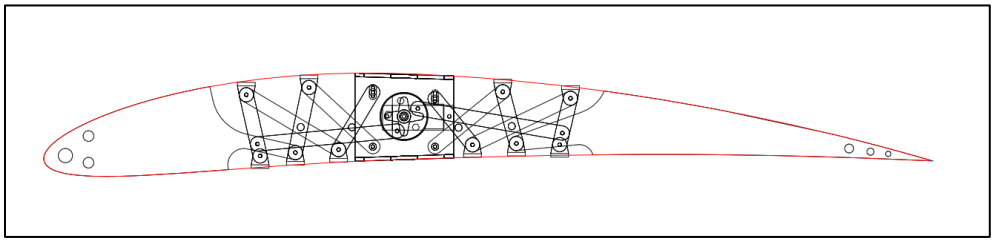

Fig. 26 The shape difference between the morphing wing rib and NACA 5410

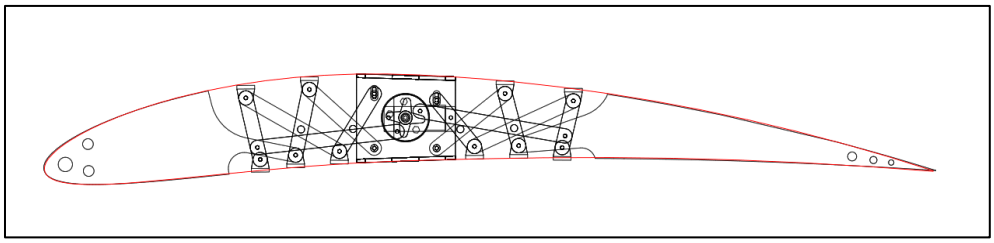

Fig. 27 The shape difference between the morphing wing rib and NACA 6410

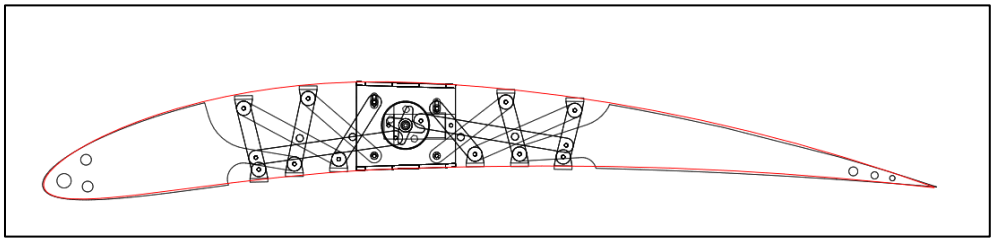

Fig. 28 The shape difference between the morphing wing rib and NACA 7410

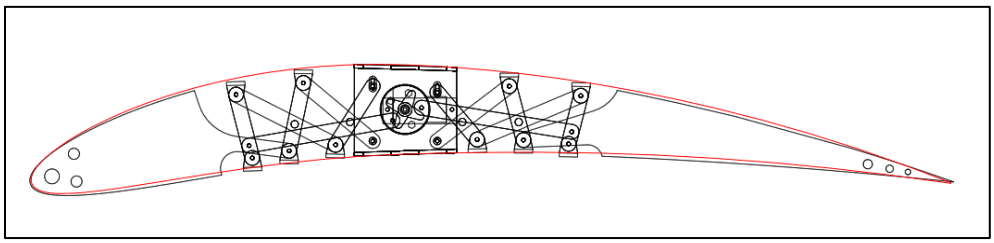

Fig. 29 The shape difference between the morphing wing rib and NACA 8410

The shape differences can be confirmed by Fig. 23, Fig. 24, Fig. 25, Fig. 26, Fig. 27, Fig. 28 and Fig. 29. In these figures, the red lines are the target airfoils and the black lines are represented as the morphing wing rib.

The design condition was that the camber had to be changed while the chord length was constant. Since the deployable scissor structure deploys as the links are folded and unfolded, the chord length can not remain constant during the deformation. However, in the case of the greatest difference from the reference chord length, it has a difference of less than 1%, so it can be seen that it is deformed while maintaining the same chord length. Furthermore, the ribs can deform independently by the actuator, so the wing can perform as a twist morphing wing, as shown in Fig. 30. The simulation was conducted by multibody dynamic software Recurdyn®.

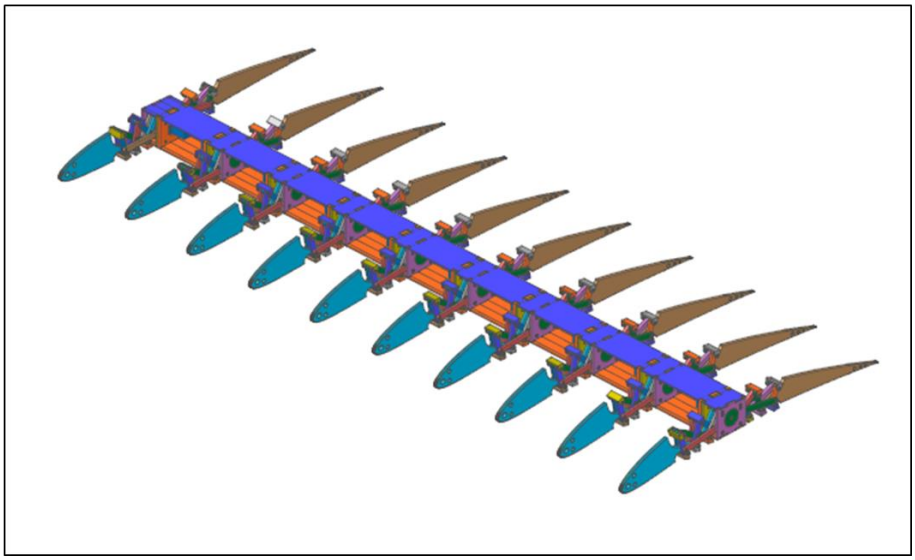

Fig. 30 Simulation of Camber Morphing Wing

2.6 Variable Camber Morphing Wing Skin

The camber morphing wing deforms by the ribs that can have various cambers. The skin covering the wing has to be flexible to alter the shape as the wing deforms. In contrast, the skin must withstand a given aerodynamic force. Therefore, the skin has to require low in-plane and high out-of-plane stiffnesses. During the morphing deformation, the skin is flexible the most in the chordwise, not in the spanwise. In other words, the skin has a different characteristic as the directions. Thus, the composite material is proper to apply the camber morphing wing skin.

2.6.1 Analysis of Camber Morphing Wing Skin

The composite material used for the analysis consists of the carbon fiber and silicone matrix. The fiber's elastic modulus is represented as $\mathrm{E_f}$, and the matrix's modulus is represented as $\mathrm{E_m}$. The volume fraction of the fiber(V_f) is assumed to be 0.6, and the volume fraction of the matrix(V_m) is 0.4.

$$E_1 = \mathrm{E_f} V_f + E_m V_m \tag{9}$$

$$E_2 = \frac{1}{\frac{V_f}{E_f} + \frac{V_m}{E_m}} \tag{10}$$

The properties of the composites are calculated using several formulas. The elastic moduli of the composite are determined through Eq.(9) and Eq.(10) [5].

The analysis was conducted using the multibody dynamic software Recurdyn®. The skin is assumed as an isotropic material using the chordwise direction of the elastic modulus. The wing structure is composed of seven ribs and is mostly made of plywood. All of the initial morphing wing ribs form the NACA 5410 having the mediate camber value.

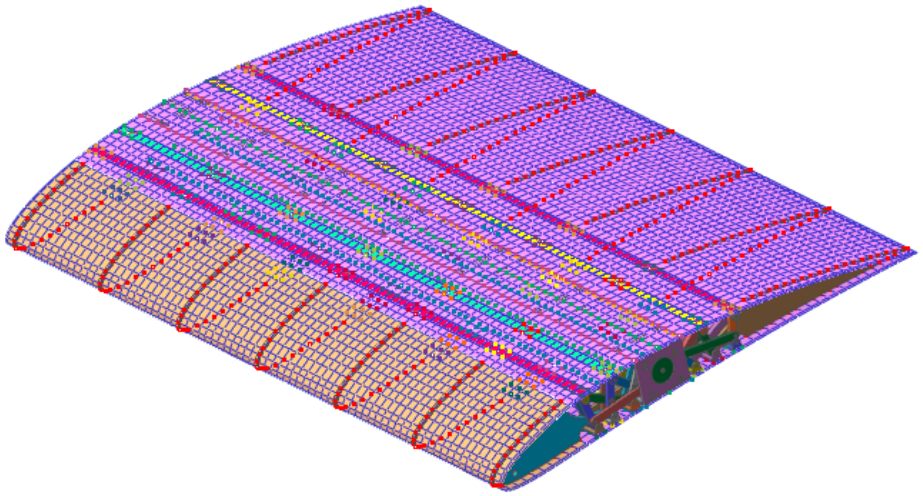

Fig. 31. Camber Morphing Wing Skin

The skin's mesh type consists of shell4 quad4 elements and has mostly the same size, but the skin at the leading edge part with large curvature was split smaller. The skin is fixed with the leading edge part, the trailing edge part, spar, and the offset parts.

Simulations were performed for the ribs implementing all target airfoils and all NACA 8410. First, each of the ribs represents different target airfoils. In other words, it represents when the wing performs as a twist morphing wing. The rib closest to the fuselage was formed as NACA 2410, and in turn, the camber of the target airfoil was enlarged. Therefore, the farthest rib from the fuselage was formed as NACA 8410. The von Mises stress distribution and von Mises strain distribution can be obtained through the simulation, as shown in Fig. 32 and Fig. 33. The maximum stress is 4.06MPa and the maximum strain is 0.935. At this simulation, it was confirmed that wrinkles occurred on the skin from the ribs having a camber value smaller than NACA 5410.
When all ribs are deformed to NACA 8410, the von Mises stress distribution and the von Mises strain distribution are shown in Fig. 34 and Fig. 35. It was confirmed that the skin has relatively high stress in the leading edge part. Moreover, strain distribution represented a similar pattern to stress distribution.
Through the simulations, the behavior of the skin can predict during the morphing deformation.

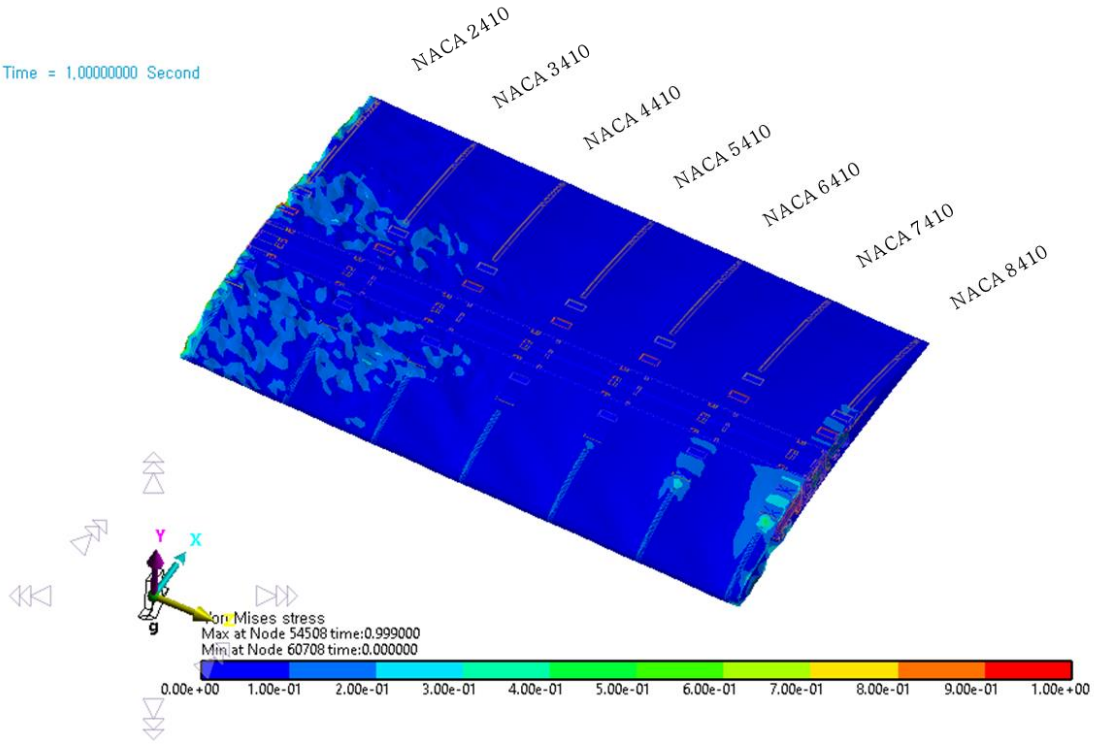

Fig. 32. Stress distribution of Skin for all target airfoils

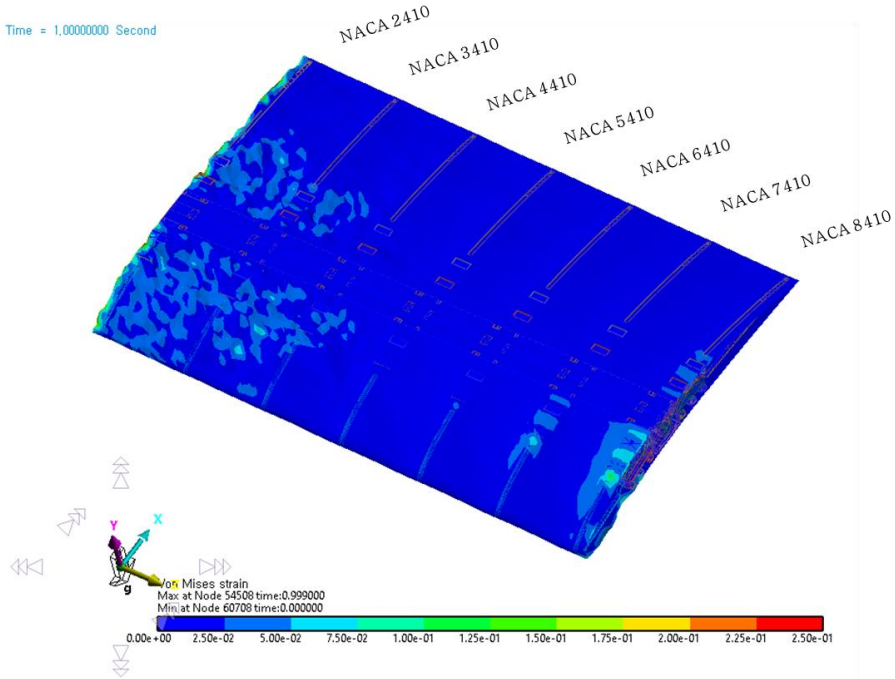

Fig. 33 Strain distribution of Skin for all target airfoils

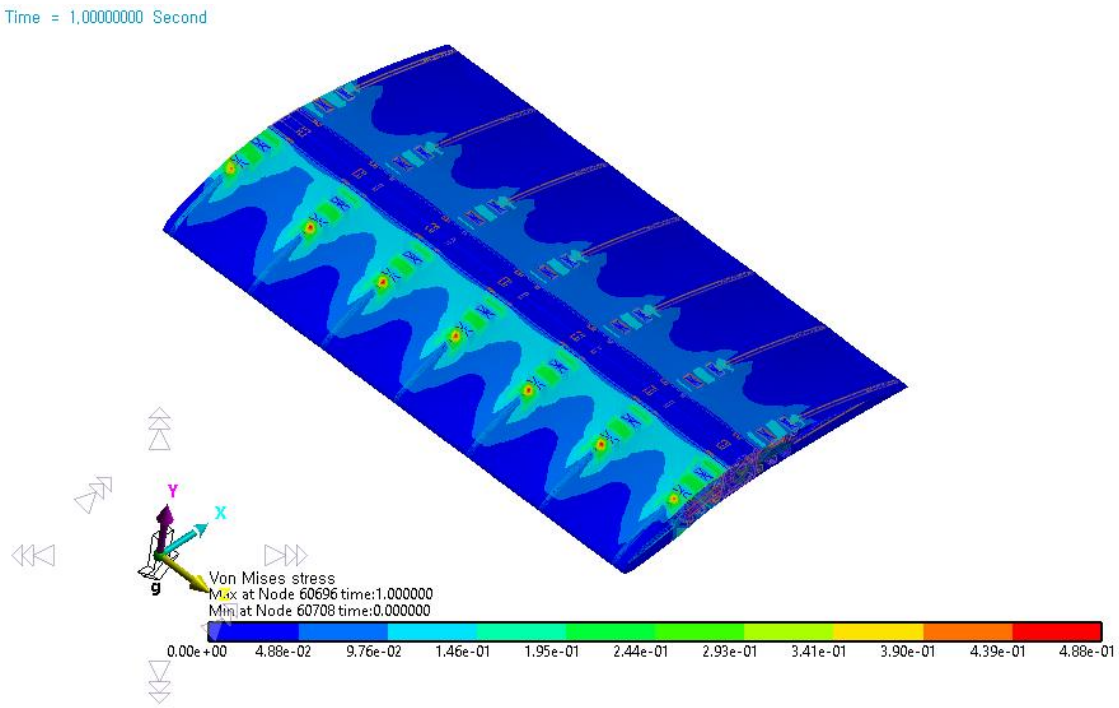

Fig. 34 Stress distribution of Skin for NACA 8410

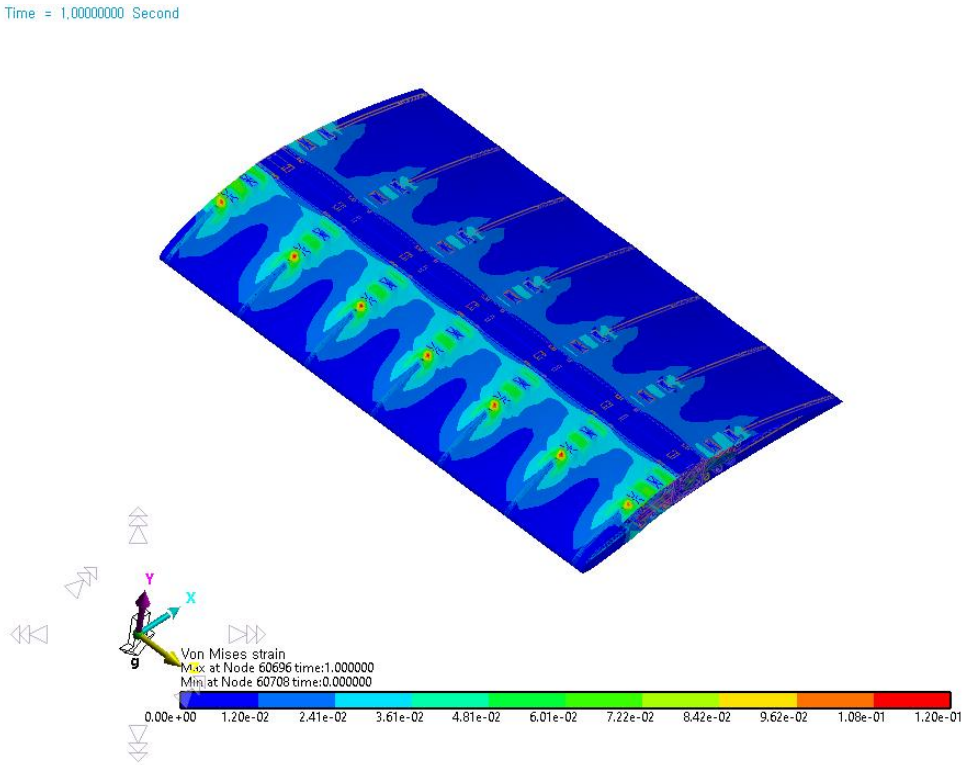

Fig. 35 Strain distribution of Skin for NACA 8410

2.7 Manufacturing of Variable Camber Morphing Wing

The ribs are mostly made of plywood and connected using stainless steel screws. The wing is manufactured based on the designed model. There are differences between the designed rib model and the manufactured rib. The designed rib's links unmarked in Fig. 36 are located symmetrically by the links red-marked in Fig. 36. Due to the thickness of the screws and the wood, the assembly arrangements are different, as shown in Fig. 37 and Fig. 38. The differences in arrangement and thickness did not cause a problem during the operation.

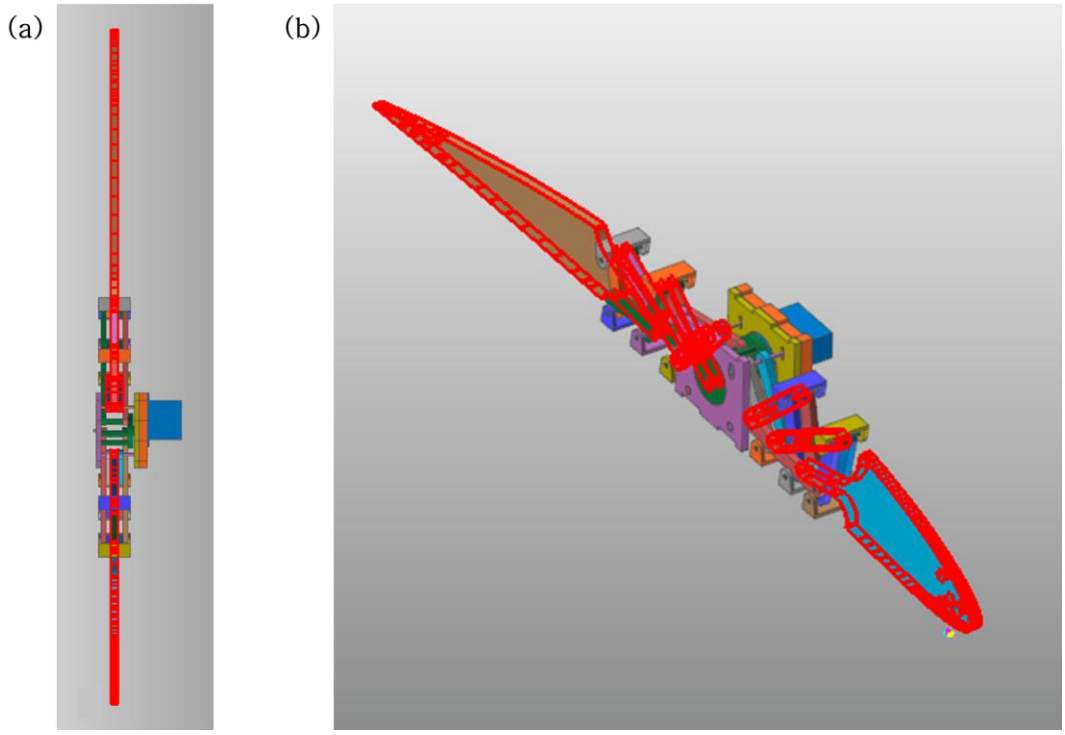

Fig. 36 Links having the same position with the leading edge part and the trailing edge part

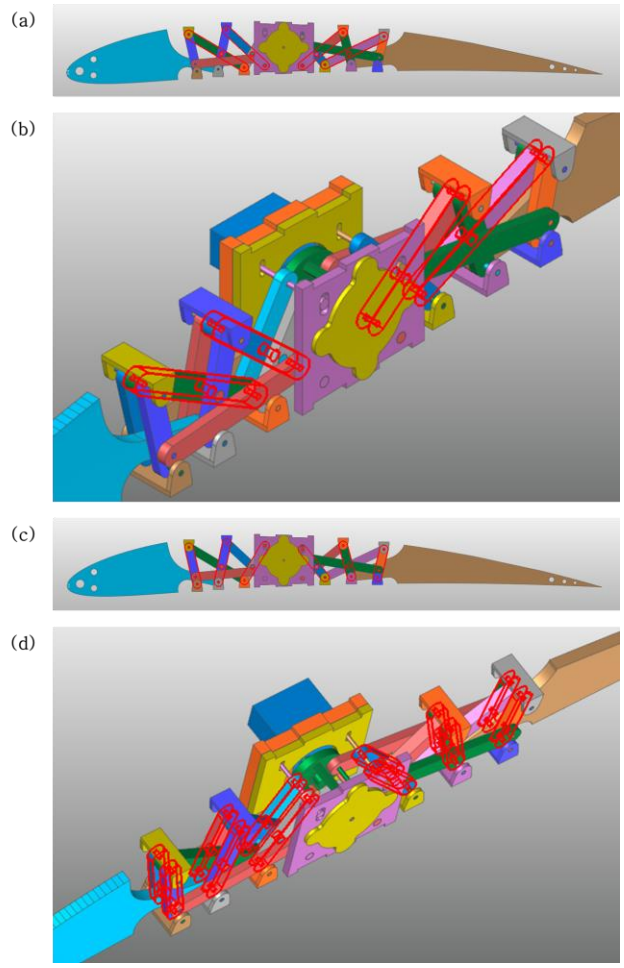

Fig. 37 The designed rib's arrangement

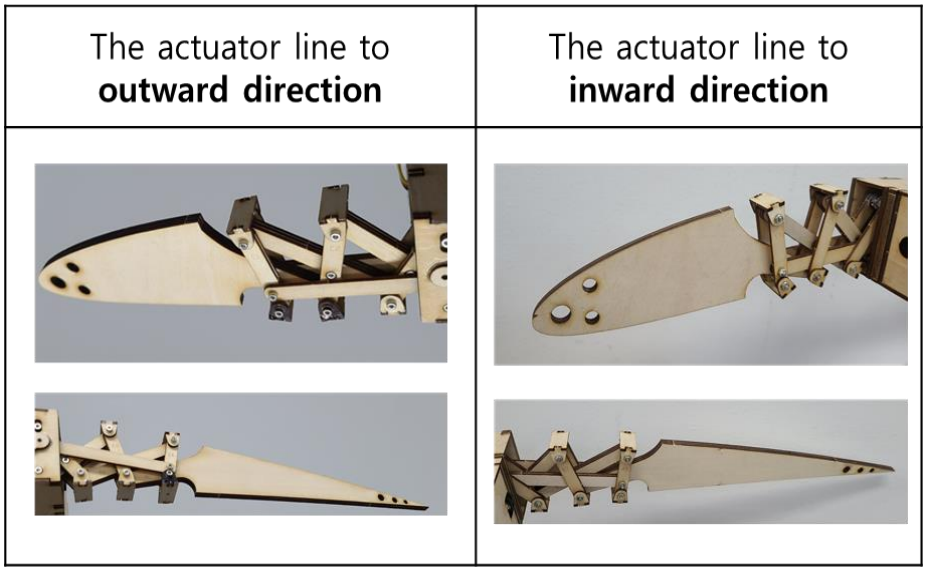

Fig. 38 The manufactured rib's arrangement

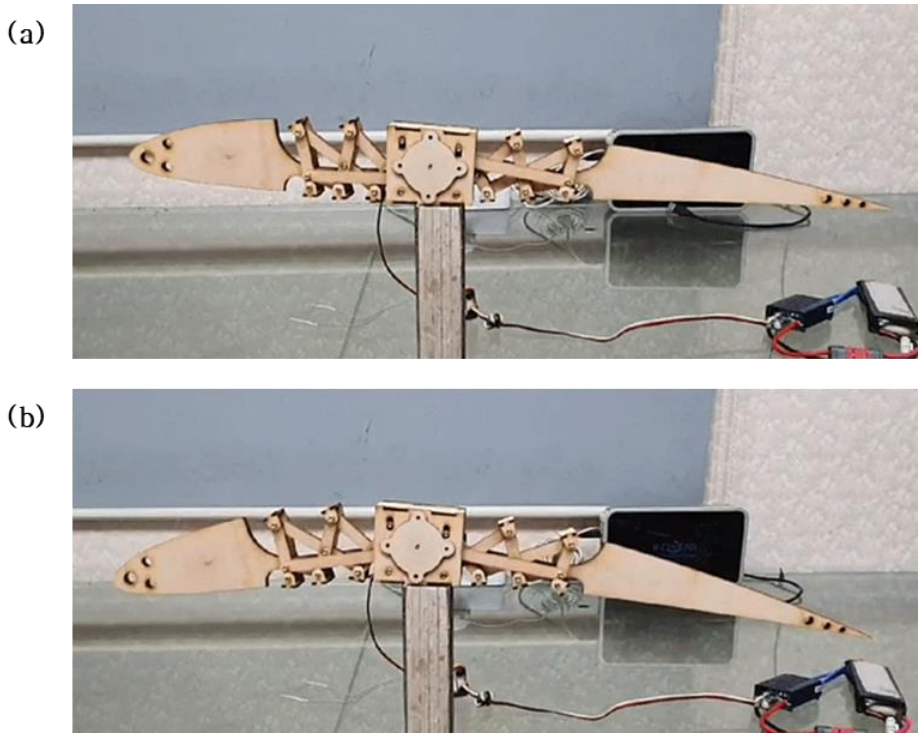

Fig. 39 (a)NACA 2410 and **(b)**NACA 8410 by manufactured Camber morphing wing rib

The reference wingspan was set as about 1.76m and composed of 14 ribs. However, the wing made part of the reference model, so the wing was manufactured to consist of ten ribs. The spacing is 85mm based on the designed wing, but the ribs' thickness is different from the designed rib. As these differences are measured, the span of the manufactured wing is about 1.1m. The chord length is identical to the designed condition as 500mm. If all the ribs are put in the same direction, the rib closet fuselage actuator is protruded. Therefore, only the actuator of this rib was connected in the reverse direction. The wire was lengthened to give the power source.

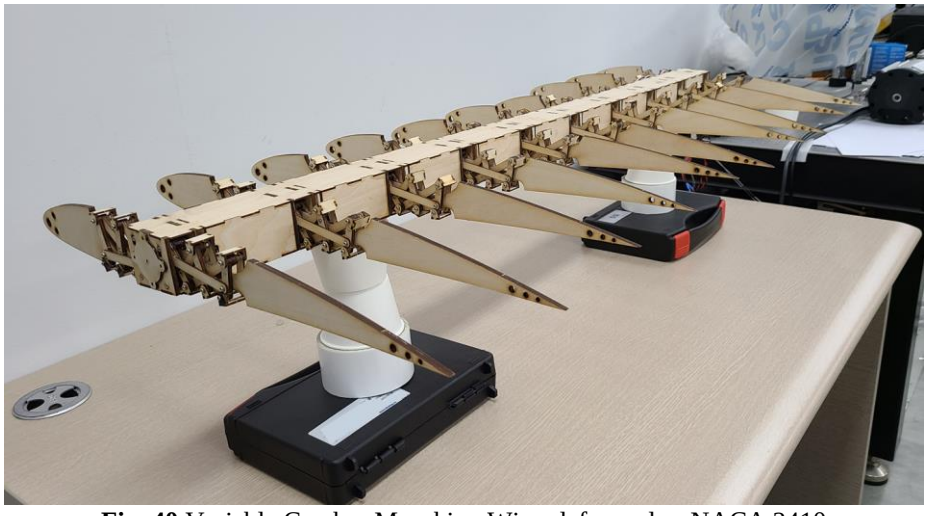

Fig. 40 Variable Camber Morphing Wing deformed as NACA 2410

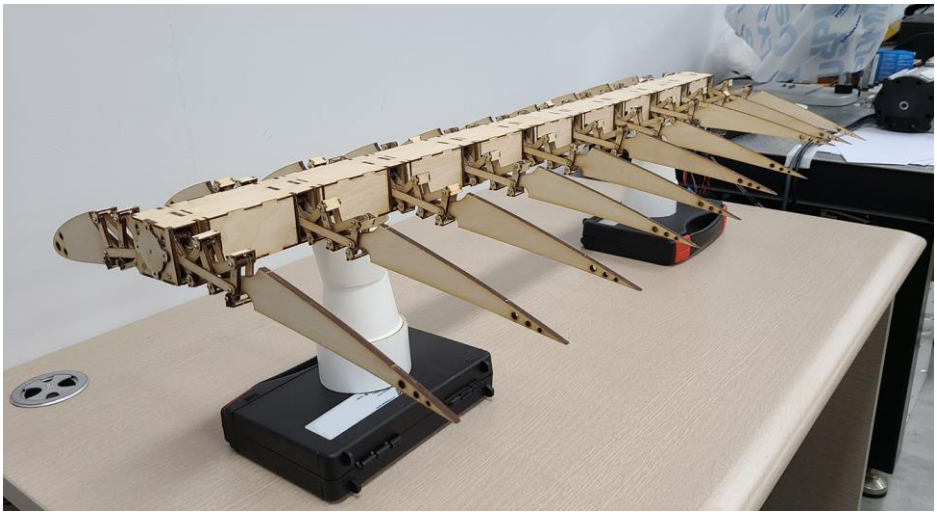

Fig. 41 Variable Camber Morphing Wing deformed as NACA 8410

Fig. 42 Variable Camber Morphing Wing deformed as a twist morphing wing

The manufactured wing is shown in Fig. 40, Fig. 41, and Fig. 42. Fig. 40 shows that all ribs form NACA 2410, and Fig. 41 shows that all ribs form NACA 8410. In Fig. 42, the ribs are having different cambers. Thus the entire wing is twisted.

3 RESEARCH ACHIEVEMENTS

3.1 Representative research achievements (Journal paper or patent)

Number	Type	Journal	Title	Remarks
1	Journal paper	AIAA	"Design Criteria for Variable Camber Compliant Wing Aircraft Morphing Wing Skin"	Accepted
2	Journal paper	Additive Manufacturing	"Characterization of Process-Deformation/Damage Property Relationship of Fused Filament Fabrication 3D Printed Materials"	Accepted
3	Journal paper	AIAA	"New Concept for Aircraft Morphing Wing Skin: Design, Modeling, and Analysis"	Accepted
4	Journal paper	International Journal of Plasticity	"Microstructure Topology Optimization by Targeting Prescribed Nonlinear Stress-Strain Relationships"	Accepted

3.2 Other research achievements (except journal paper and patent)

Number	Type	Title	Year
1	International Conference	Seongik Kim and Gunjin Yun "Design of Material with prescribed Nonlinear properties considering Material Nonlinearity" Asian Pacific Congress on Computational Mechanics (APCOM) December 18 - 20, 2019, Taipei Taiwan	2019
2	International Conference	Seongik Kim and Gunjin Yun "Topology Optimization of Elastomeric Materials for Aircraft Morphing Wing Skin" Korea-Japan Joint Seminar on Advanced Structures and Materials for Morphing Technology in Future Aircrafts November 20 - 21, 2019, Jeju Korea	2019
3	International Conference	Yeeryung Choi and Gunjin Yun "Optimal Design of Aircraft Morphing Wings Internal Mechanism by Deployable Scissor Structures" Korea-Japan Joint Seminar on Advanced Structures and	2019

		Materials for Morphing Technology in Future Aircrafts November 20 - 21, 2019, Jeju Korea	
4	International Conference	Yeeryung Choi and Gunjin Yun "Optimal Design of Scissor Strucutral Mechanism for Space Deployable Structures" The 4th International Conference on Active Materals and Soft Mechatronics, October 16 - 19, 2019, Incheon Korea	2019
5	International Conference	Hyoungjun Lim, Tomas Webbe Kerekes, Woong Yeol Joe and Gunjin Yun "Characterization and modeling of Failure Behavior of 3D Printed Materials" ICAST 2018 29th , Sep 30 – Oct 4, 2018, Seoul Korea	2018
6	International Conference	Bashir Alsaidi, W. Yeol Joe, Hangil You, Seongik Kim and Gunjin Yun "Computational Modeling and Analysis for Design of Skin Structure in Camber Morphing Wings" The 2018 Structures Congress, Aug. 27-31, 2018, Incheon Korea	2018
7	Domestic Conference	Yeeryung Choi and Gunjin Yun "Design and Manufacturing of Internal Mechanism of Camber Morphing Wing Rib by Deployable Scissor Structures" KSAS Spring Conference July 8 - 10, 2020, Goseong Korea	2020
8	Domestic Conference	Yeeryung Choi and Gunjin Yun "Optimal Design of Aircraft Morphing Wing's Internal Mechanism by Deployable Scissor Structures" KSAS Fall Conference November 20 - 23, 2019, Jeju Korea	2019
9	Domestic Conference	Hangil You and Gunjin Yun "New UAV Morphing Wing Skins using Gripper-pin Structure: Design, Modeling and Analysis" KSAS Spring Conference April 17 – 20, 2019, Buan Korea	2019
10	Domestic Conference	Seongik Kim and Gunjin Yun "Multiscale Topology Optimization of Mesostructure for Aircraft Morphing Wing Skin by Inverse Homogenization", KMSM Symposium December 20 – 21, 2018, Jeonju Korea	2018
11	Domestic Conference	Hangil You and Gunjin Yun "Finite Element Analysis of Variable Camber Compliant Wing Skins", COSEIK Symposium November 15 – 16 2018, Jeju Korea	2018
12	Domestic Conference	Seongik Kim, Hangil You and Gunjin Yun "Topology Optimization of Mesostructure of Aircraft Morphing Wing Skin by Inverse	2018

		Homogenization", COSEIK Symposium November 15 – 16, 2018, Jeju Korea	
13	Domestic Conference & Award	Hangil You, Seongik Kim, W. Yeol Joe and Gunjin Yun "Design of Advanced Composite Skins for Morphing Wings-Analysis, Manufacturing and Control" 2018 KSAS Summer Workshop, July 3-4, 2018, Busan Korea 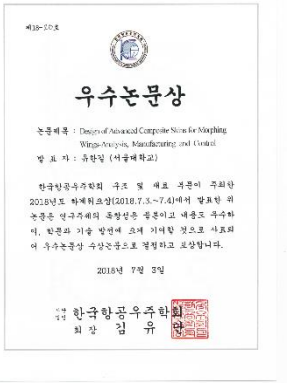 우수논문상 논문제목 : Design of Advanced Composite Skins for Morphing Wings-Analysis, Manufacturing and Control 발 표 자 : 유한일 (서울대학교) 한국항공우주학회 우주 및 재료 분과의 주최한 2018년도 하계워크샵(2018.7.3.~7.4)에서 발표한 위 논문은 연구목적의 독창성을 인정하고 대상으로 우수하며, 학술과 기술 발전에 크게 기여할 것으로 사료되어 우수논문상 수상논문으로 결정하고 포상합니다. 2018년 7월 3일 한국항공우주학회 회장 심 유	2018
14	Domestic Conference	Seongik Kim, Hangil You, Bashir Alsaidi, Muhammad Akbar, W. Yeol Joe and Gunjin Yun "Preliminary Skin Design of Variable Camber Morphing Wing through Material Properties" 2018 KSAS Spring Conference, April 18-21, 2018, Goseong Korea	2018

4 KOREA – JAPAN JOINT SEMINAR

Korea-Japan joint seminar on morphing wing technology was held in Jeju island, Korea for 3 days from November 20,2019. The seminar was organized by Professor Gunjin Yun and Professor Tomohiro Yokozeki from University of Tokyo.

There were 35 participants (Korea : 19, Japan : 15, USA : 1). The seminar included 9 presentations in Korea and 12 presentations in Japan, including presentations by Professor Gunjin Yun of "Design Criteria for Morphing Wing Skin and Lattice Structure" and our team's "Topology Optimization of Elastomeric Materials for Aircraft Morphing Wing Skin" and "Optimal Design of Aircraft Morphing Wing's Internal Mechanism by Deployable Scissors Structures" presentations. Presentations were conducted to research new materials for morphing and morphing structure design through structural optimization and morphing mechanism proposal through new ideas. Also, an US researcher was also invited to the seminar through this project. The joint seminar sponsored by the National Research Foundation of Korea, the Japan Society for the Promotion of Science, was a beneficial venue for academic exchanges between Korea and Japan, focusing on morphing technology.

5 REFERENCE

1. Joo, J.J., et al. *Variable Camber Conpliant Wing - Design*. in *AIAA SciTech Forum 23rd AIAA/AHS Adaptive Structures Conference*. 2015. Kissimmee, Florida.
2. Joo, J.J., C.R. Marks, and L. Zientarski. *Active wing shape reconfiguration using a variable camber compliant wing system*. in *Proceedings of 20th International Conference on Composite Materials*. July 19-24 2015. Copenhagen.
3. Langbecker, T., *Kinematic Analysis of Deployable Scissor Structure S.* International Journal of Space Structures, 1999. **14**(1): p. 1-15.
4. De Temmerman, N., *Design and analysis of deployable bar structures for mobile architectural applications*. 2007, Ph. D. thesis, Vrije Universiteit Brussel, Brussels, Belgium.